Supporting Information for

Small alkaline-earth-based core/shell nanoparticles for efficient upconversion

Stefan Fischer[1]*, Randy D Mehlenbacher[1], Alice Lay[2], Chris Siefe[1], A. Paul Alivisatos[3,4,5,6], and Jennifer A. Dionne[1]*

[1]Department of Materials Science and Engineering, Stanford University, 496 Lomita Mall, Stanford, CA 94305, USA

[2]Department of Applied Physics, Stanford University, 348 Via Pueblo Mall, Stanford, CA 94305, USA

[3]Materials Sciences Division, Lawrence Berkeley National Laboratory, Berkeley, California 94720, USA

[4]Department of Chemistry, University of California Berkeley, Berkeley, California 94720, USA

[5]Department of Materials Science and Engineering, University of California Berkeley, Berkeley, California 94720, USA

[6]Kavli Energy NanoScience Institute, Berkeley, California 94720, USA

Table of Contents

1 Synthesis

1.1 Chemicals

Calcium carbonate (99.99%, Mallinckrodt), Strontium carbonate (99.9%, Sigma-Aldrich), and Barium hydroxide monohydrate (98%, Sigma-Aldrich) were used to make trifluoroacetate precursors. All rare-earth oxides (99.9%) and trifluoroacetic acid (99%) were purchased from Alfa Aeser. Sodium oleate was purchased from TCI America. Yttrium acetate hydrate (99.9%), sodium trifluoroacetate (98%), sodium hydroxide (≥98%), ammonium fluoride (≥99.9%), and oleic acid (90%) were purchased from Sigma-Aldrich. Oleylamine (OLA, 70% tech. grade), 1-octadecene (ODE, 90% tech grade), and ethanol were purchased from Acros. All other organic solvents were purchased from Fisher Scientific. All chemicals are used as received without further purification.

1.2 Precursor preparation

The trifluoroacetate (TFA) precursor solutions are prepared by the following standard procedure.[1] Here, we describe the standard method to form Y-TFA from Y_2O_3. Making other rare-earth (Ln) and alkaline-earth (M) metal precursors follows the same general procedure with slight variations in the amount of trifluoroacetic acid and water necessary to dissolve the Ln oxides or the M carbonates or hydroxides. Typically, less water and trifluoroacetic acid is necessary to form the M-TFAs and the reaction already starts at room temperature but we still heated the solution to 90°C before drying to make sure the M-TFAs are formed.

First, a ratio of 1 mmol Y_2O_3, in 1 mL 99% trifluoroacetic acid and 5 mL distilled water is added in a 3-neck flask. This mixture is heated to 90°C in an oil bath using a condenser column to prevent evaporation. After all the Y_2O_3 is completely dissolved and the solution is transparent, the water and the remaining trifluoroacetic acid are evaporated at 65°C to obtain a white powder of 2 mmol yttrium trifluoroacetate. Next, we add 3 mL oleic acid (OA) and 3 mL 1-octadecence (ODE) into the flask for a concentration of 3 mL per 1 mmol. For the M-TFAs we use 1 ml OA and 1.5 ml ODE for 1 mmol of M-TFAs. The mixture is put under vacuum using a Schlenk line. The solution is then slowly heated to 120°C to obtain a clear, slightly yellow or colored solution depending on the Ln-TFA. We cycle between vacuum and argon at least 3 times to remove any residual water and oxygen. After cooling to ~50°C, we transfer the slightly viscous precursor liquids into vials for later use.

Sodium trifluoroacetate ($NaCF_3CO_2$, Na-TFA) precursor solutions are made in a similar way. We mixed ratios of 1 mmol of Na-TFA with 1.5 mL OA and 1.5 mL ODE in a 3- neck flask. This solution is heated carefully to 120°C under vacuum. We cycle between vacuum and argon at least 3 times to dissolve the Na-TFA and remove any residual water and oxygen. After the Na-TFA is completely dissolved and the solution became clear (slightly yellow) the heating is turned off. The precursor solution is transferred into vials at ~50°C.

Y-oleate precursor solution is prepared by dissolving 1 mmol Y-acetate salts in 2 mL OA and 2 mL ODE under vacuum by slowly heating the solution up to 120°C. We cycled between vacuum and argon at least 3 times to remove any residual water and oxygen. Once all the salts are dissolved the heating mantel is removed to let the solution cool down. After cooling to ~50°C, we transfer the slightly viscous precursor liquids into vials for later use.

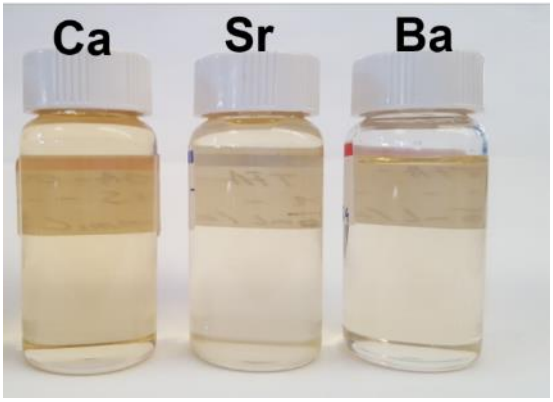

Figure S1. Alkaline-earth metal trifluoroacetates (TFAs) dissolved in oleic acid and 1-octadecence under vacuum as described in the Experimental Section and used in the core synthesis and shelling.

1.3 Synthesis of $M_{1-x}Ln_xF_{2+x}$ core UCNPs (M = Ca, Sr, Ba; Ln = Y, Lu)

The $M_{1-x}Ln_xF_{2+x}$ (MLnF) core nanoparticles are synthesized by thermal decomposition of the corresponding TFA salts. The synthesis is adopted from Chen et al. with modifications.[2] We prepared the Ln precursor solution directly from the oxides using molar percentages of 68.8% Y_2O_3 or 68.8% Lu_2O_3 with 28.4% Yb_2O_3 and 2.8% Er_2O_3.
In a typical synthesis, 1 mmol Ln- TFA solution and 1 mmol of M-TFA solutions are added in a 50 mL three-neck flask under magnetic stirring at roughly 300rpm. OA, ODE, and OLA are added to the flask to reach a total amount (including the precursor solutions) of 6mL OA, 13mL ODE, and 2mL oleylamine (OLA). After adding OLA the temperature of the mixture increases by ~6°C and the stirring was set to 1000 rpm. The mixture is then heated to 120°C under vacuum using a Schlenk line and we cycled between argon and vacuum 3-5 times. When vacuum values <40mTorr are reached the solution is heated in 10 min to

300°C under argon. Between 260-300°C the TFA salts decompose rapidly resulting in an eruption in the flask. During this decomposition some water vapor is released that may lead to further eruption if not captured through an argon flow setup using a water or oil bubbler. Residual water vapor may also be released in a closed flask system by carefully and temporarily sticking a needle into a rubber septum covering one of the flask's necks. After being at 300°C for 45 min for the Ca and Ba-based samples and 60 min for the Sr-based samples the heating mantel is removed and the mixture was allowed to cool down to room temperature. The particles are then precipitated by addition of roughly 15 mL ethanol and centrifugation at ~4,000g. After a washing step by dispersing UCNPs in hexane and adding ethanol followed by centrifugation at ~3,000g, the MnLnF core UCNPs are dispersed and stored in 10 mL cyclohexane. 2 mL of the core UCNPs are washed another 2 times and dispersed in toluene for optical characterization.

1.4 Shelling procedure for $M_{1-x}Ln_xF_{2+x}$ UCNPs

We added 0.75 mmol (7.5 mL) of the washed cores in a 100 mL 3-neck flask with 7.5 mL OA and 15mL ODE with magnetic stirring with ~500 rpm. After evaporating the hexane at 65°C with two open necks the solution was carefully put under vacuum using a Schlenk line. The stirring is increased to 100 rpm and flask is heated to 120°C. We cycled between argon and vacuum 3-5 times before heating the solution to 300°C under argon. At 270°C we started dropwise injection of the shell precursor through a septum using a syringe pump. The shell precursor was made by mixing the Y-oleate and corresponding M-TFA solutions with a 1:1 molar ratio. We injected the shell precursor with a rate of 6 mmol/hr per each mmol of core material in the solution (here 4.5 mmol/hr). This means that the nanoparticles will grow in volume by a factor of 6 in one hour. The precursor solution concentration of 6.5 mL/mmol translates to a volumetric injection rate of 29.3 mL/hr. Using the core diameter, we calculated the amount of shell precursor necessary to obtain shell thicknesses of 1, 2, 3, 5, and 7 nm. After injection of the corresponding shell precursor amount, we waited 5 min before taking an aliquot using a glass syringe and continuing the shelling procedure for the next sample. The measured shell thicknesses vary between the samples due to uncertainty in the core diameter, inequal amounts of aliquots taken out of the hot solution, and varying stoichiometric ratios of the different MLnF UCNPs. The samples are precipitated with addition of ethanol and centrifuging at ~3,000g. All samples are washed 3 times by dispersing in hexane, precipitating in ethanol, and collecting via centrifugation (3,000g) before dispersing in toluene. Moreover, we washed the MLnF core/shell UCNPs by a phase separation process using water to remove oleate residuals forming foam in the toluene dispersed samples. We mixed the toluene sample with water and took the clear toluene volume from the top containing most of the MLnF UCNPs (Figure S2). Because of the

additional washing the concentration of MLnF UCNPs in the final solution is lower than the one for the NaGdF samples, resulting in lower absorptance of the samples during UCQY measurements as shown in Figure 2a. We repeated this procedure twice, washed the sample once more by precipitation using ethanol and centrifugation, and finally dispersed the core/shell UCNPs in toluene.

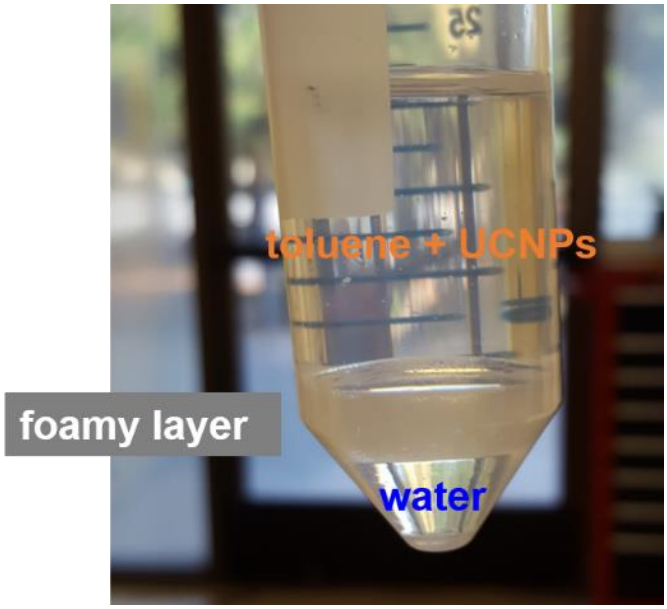

Figure S2. Example of washing step of core/shell MLnF UCNPs by phase separation using toluene and water to remove residual substances from the synthesis, such as oleates, which were not washed out during the preceding ethanol, hexane, and centrifugation steps.

1.5 Synthesis and shelling of β-$NaGdF_4$ core/shell UCNPs

The NaGdF core/shell UCNPs are prepared as reported in literature with slight modifications.[3] In short, Ln-oleates are formed in a 100 mL 3-neck flask by adding 2 mmol of Gd, Yb, and Er-acetate with ratio 0.78, 0.20, and 0.02, respectively. We added 14 mL OA and 30 mL ODE before applying vacuum using a Schlenk line. After dissolving all the acetates at 120°C, the solution is cooled down to 70°C and we added 5 mmol of Na-oleate and 9 mmol of NH_4F directly into the flask. We dissolve the Na-oleate and NH4F by cycling between argon and vacuum multiple times and heating slowly to 120°C. Once the NH_4F is sufficiently dissolved the mixture is heated in 10 min to 300°C with ~20°C/min and stirring at 1000 rpm. After 45 min at 300°C the solution is cooled down to room temperature. The core NaGdF UCNPs are collected by addition of ethanol and centrifugation (4,000g). The UCNPs for shelling are washed one more time by dispersing in hexane, precipitation using ethanol, and collected by centrifugation (4,000g) before dispersing them in hexane at a concentration of 0.1M. 0.2 mmol of the NaGdF cores are washed 3 more times with hexane and ethanol before dispersing in toluene for characterization.

For NaGdF core/shell samples, 0.75 mmol of the cores are mixed with 7.5 mL OA and 15 mL ODE in a 100 mL 3-neck flask. After evaporating hexane at 65°C with two open necks the solution is carefully put under vacuum and heated to 120°C using a Schlenk line. We cycled between argon and vacuum 3-5 times before heating the solution to 300°C with ~20°C/min under argon. We used a sequential shelling process by injection of Na-TFA and Y-TFA precursor solution as described in literature with a 6 min waiting period between injection.[1] As for the MnLnF core/shell UCNPs, we calculated the amount of shell precursors to obtain shell thicknesses of 1, 2, 3, 4, and 6 nm and taking aliquots along the shelling process. After cooling down to room temperature the NaGdF core/shell UCNPs were collected by addition of ethanol and centrifugation (4,000g). Samples were washed 3 times by dispersing in hexane, precipitation by adding ethanol, and centrifugation (3,000g) before dispersing in toluene for characterization.

Table S1. Molar amounts per injection of mixed Y-TFA and Na-TFA precursor solutions to grow inert β-$NaYF_4$ shells around the β-$NaGdF_4$: 20% Yb^{3+}, Er^{3+} core UCNPs.

	CS1	CS2	CS3	CS4	CS5
Amount of precursor injected (mmol)	1× 0.20 4× 0.25	2× 0.25 4× 0.30	2× 0.30 3x 0.35	4× 0.35	4× 0.40

1.6 Equivalent doping considerations and calculations

Ideally, we would like all our samples to have the same distance distribution between the dopants Yb^{3+} and Er^{3+}. The distance distribution between the dopants depends on the crystal structure, lattice parameters, and doping concentration. It is not possible to exactly match distance distributions for different crystal structures and lattice parameters. Therefore, we used the concept of equivalent doping which results in same average distance between the dopants in different crystal structures and lattice parameters.

The average distance between the rare-earth ions (d_{Ln}) of hexagonal-phase $NaYF_4$ can be calculated from the volume of the unit cell ($V_{\mathrm{unit,cell}}$), the number of rare-earth ions per unit cell (Z_{Ln}), and the doping level ([doping]) by $d_{\mathrm{Ln},\beta-NaYF_4} = \sqrt[3]{\frac{V_{\mathrm{unit,cell}}}{Z_{\mathrm{Ln},\beta-NaYF_4}\,[\mathrm{doping}]}} = \sqrt[3]{\frac{a^2 b \sin 60°}{Z_{\mathrm{Ln},\beta-NaYF_4}\,[\mathrm{doping}]}}$. For cubic crystal structures the average distance between rare-earth

ions is given by $d_{\mathrm{Ln,cubic}} = \sqrt[3]{\frac{V_{\mathrm{unit,cell}}}{Z_{\mathrm{Ln,cubic}} \cdot [\mathrm{doping}]}} = \sqrt[3]{\frac{a^3}{Z_{\mathrm{Ln,cubic}} \cdot [\mathrm{doping}]}}$. An equivalent doping in a cubic $MLnF_5$ crystal structure that results in a similar average distance between rare-earth ions for a certain doping level in β-$NaYF_4$ is determined by $[\mathrm{doping}] = \frac{a^3}{Z_{\mathrm{Ln}} \cdot {d_{\mathrm{Ln},\beta-NaYF_4}}^3}$. We used the lattice parameters from reference powder diffraction patterns (pdf) to calculate the equivalent doping. For β-$NaYF_4$ we used pdf 04-017-6069 with $a = b = 5.969$ Å, $b = 3.503$ Å, and $Z_{\mathrm{Ln}} = 1.5$ because of unit cell $Na_{1.5}Y_{1.5}F_6$. For $BaYF_5$ we used pdf 04-018-2140 with $a = b = c = 5.89$ Å, $Z_{\mathrm{Ln}} = 2$ because of a number of atoms per unit cell Z = 4 and a unit cell of $Ba_{0.5}Y_{0.5}F_{2.5}$. We used these lattice parameters to determine the doping level of 28.4% Yb^{3+} and 2.8% Er^{3+} of all alkaline-earth rare-earth fluride samples in our study, which is equivalent to a doping concentration of 20% Yb^{3+} and 2% Er^{3+} in β-$NaGdF_4$.

We would like to point out that the stoichiometric ratio varies between the core MLnF samples and are different than the 1:1 ratio of M:Ln ($M_{1-x}Ln_xF_{2+x}$ with M = Ba, Ln =Y, and x = 0.5) which we assumed in the doping concentration calculations above. The various stoichiometric ratios result in different equivalent doping concentrations as the lattice sites for M and Ln are interchangeable. Instead of considering the doping concentration of Yb^{3+} and Er^{3+} for the sum of all Ln cations, we can use the doping concentration of all cations, sum of Ln and M, to calculate an equivalent doping concentration that is independent of the stoichiometric ratio. This approach is useful for post-synthesis characterization but currently does not help to increase accuracy of the doping concentration in the synthesis due to unknown stoichiometric ratio of the final product.

Moreover, Ca- and Sr-based samples have shorter lattice parameters than the Ba-based samples resulting in lower equivalent doping levels compared to $BaYF_5$. To account for all these issues, we calculate the ratio of the cation doping of Yb^{3+} and Er^{3+} over all cations (M and Ln) by applying $Z_{\mathrm{Ln}} = Z$ in the equation above. The cation doping to obtain similar average distances between Yb^{3+}/Er^{3+} as in β-$NaGdF_4$: 20% Yb^{3+}, 2% Er^{3+} are 11.8%/1.2% for CaYF, 12.9%/1.3% for SrYF, and 14.2%/1.4% for BaYF. The calculated cation doping levels are also shown in Table S2 in comparison to the experimentally determined cation doping levels from ICP-OES measurements. We used pdf 04-005-9811 with a = b = c = 5.70 Å and Z = 4 for SrYF and pdf 04-005-9810 with a = b = c = 5.535 Å and Z = 4 for CaYF.

Table S2. Atomic ratio of cations in the core nanoparticles as measured by ICP-OES. The ratio of alkaline-earth to rare-earth ions (M:Ln) is directly calculated from the atomic ratio. The cation doping from ICP-OES is compared to the targeted cation ratio for similar average distance between the dopant as outlined in the text above.

Material	Atomic ratio of M and Ln ions (%)							Ratio	Cation doping (experimental)	Cation doping (targeted)
	Ca	Sr	Ba	Lu	Y	Yb	Er	M:Ln	Yb/Er (%)	Yb/Er (%)
CaYF	62.6	0.2	0.0	0.0	28.0	8.3	0.8	1.69	8.3/0.8	11.8/1.2
CaLuF	64.4	0.2	0.0	23.6	0.0	10.7	1.0	1.83	10.7/1.0	11.8/1.2
SrYF	1.1	59.0	0.0	0.0	29.5	9.4	0.9	1.51	9.4/0.9	12.9/1.3
SrLuF	0.1	60.2	0.0	26.4	0.0	12.1	1.1	1.52	12.1/1.1	12.9/1.3
BaYF	1.3	0.4	52.9	0.0	34.0	10.4	1.1	1.20	10.4/1.1	14.2/1.4
BaLuF	0.1	0.4	53.8	30.2	0.4	13.8	1.3	1.19	13.8/1.3	14.2/1.4
NaGdF	Na = 48.0			Gd = 41.6		9.3	1.1		9.3/1.1	10.0/1.0

2 Materials characterization

2.1 X-ray diffraction (XRD) patterns

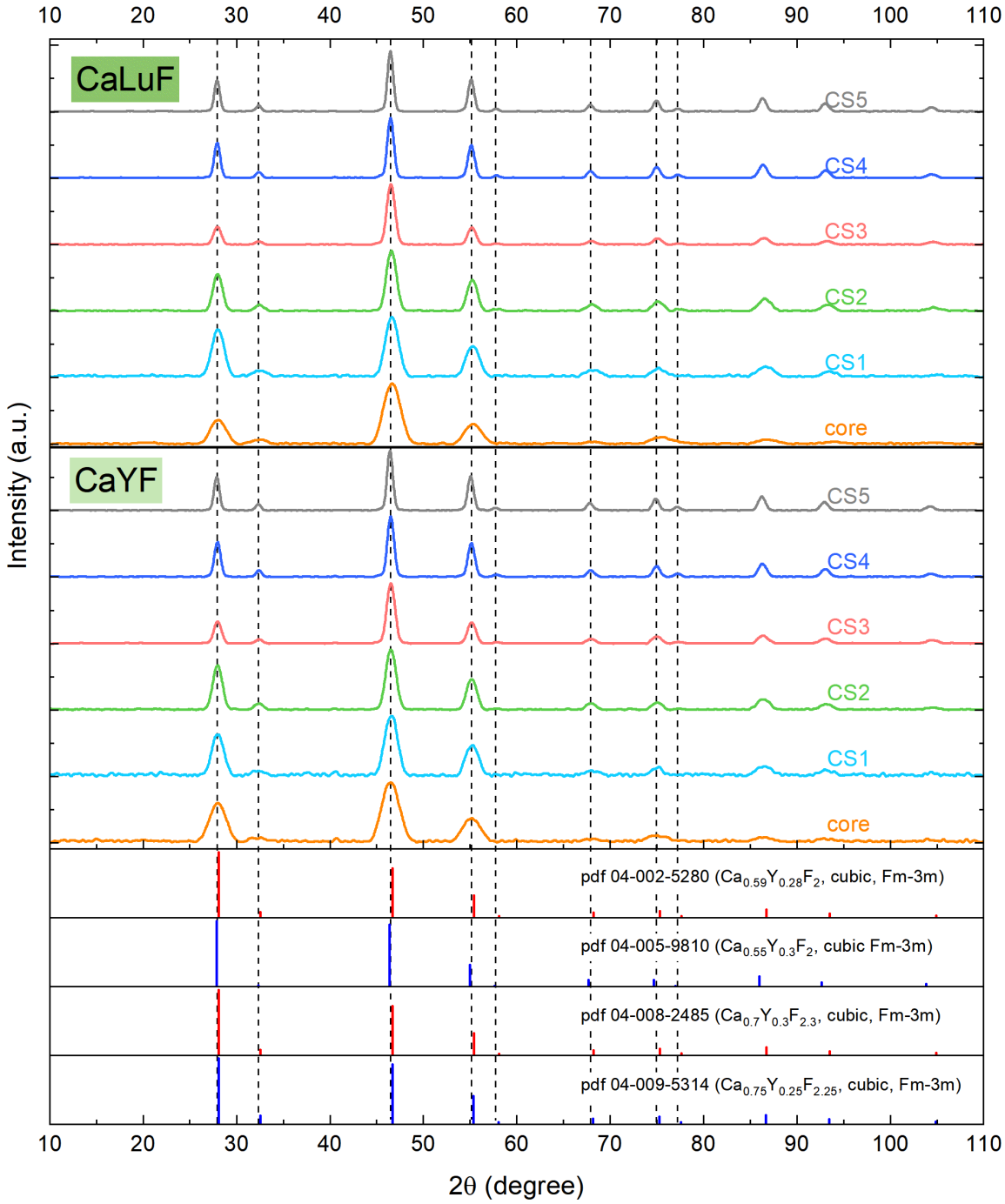

Figure S3. XRD patterns of CaYF and CaLuF samples. Due to the small size of the UCNPs the XRD peaks are broadened. The XRD peaks become sharper with increasing size due to increasing shell thickness. For a large range of stochiometric ratios, the XRD patterns are almost identical for same crystal structure and phase group as shown by different reference powder XRD pattern (pdf). Dashed lines are centered at the peak positions of CS5.

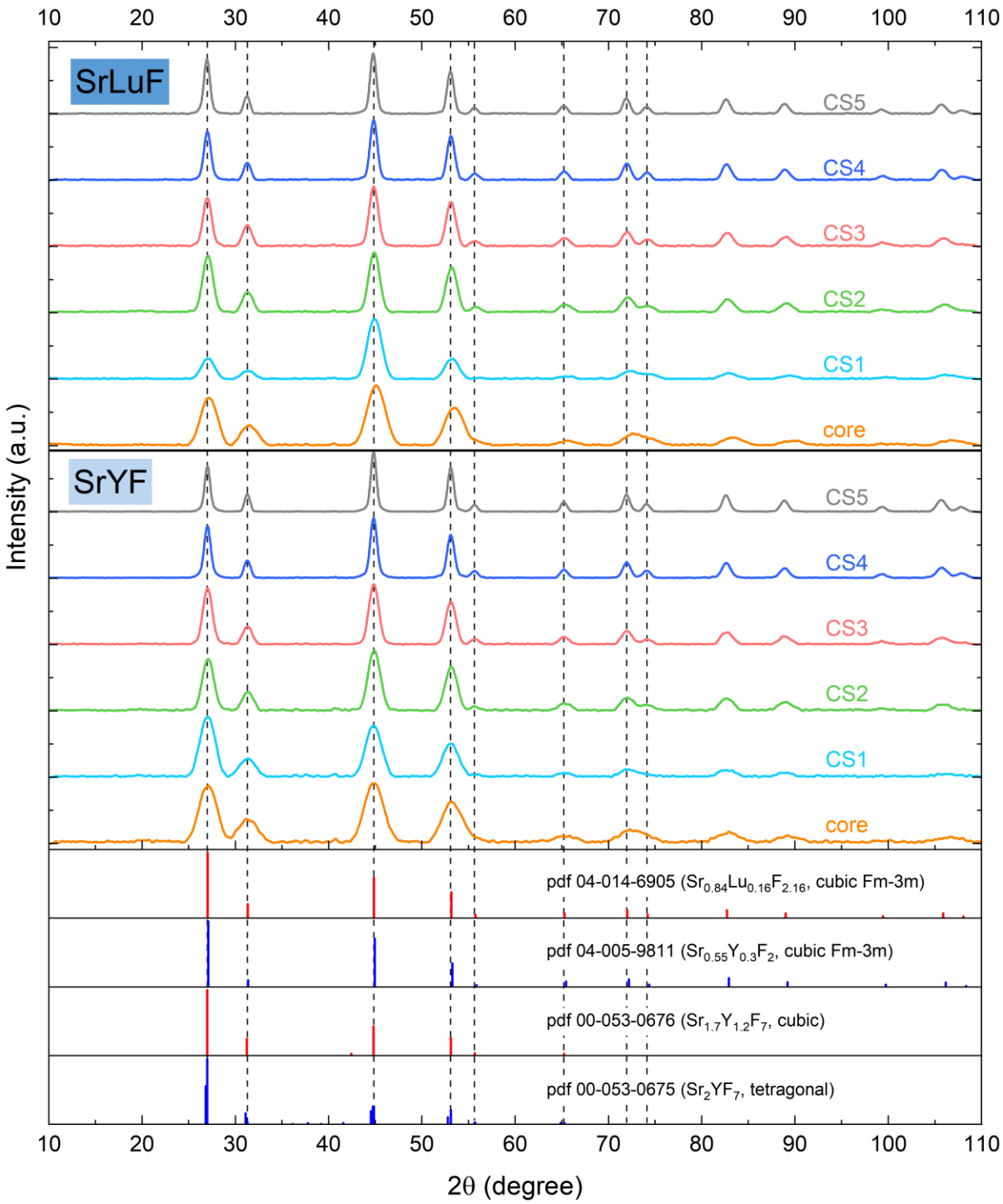

Figure S4. XRD patterns of SrYF and SrLuF samples. Due to the small size of the UCNPs the XRD peaks are broadened. The XRD peaks become sharper with increasing size due to increasing shell thickness. For a large range of stochiometric ratios, the XRD patterns are almost identical for same crystal structure and phase group as shown by different reference powder XRD pattern (pdf). Dashed lines are centered at the peak positions of CS5.

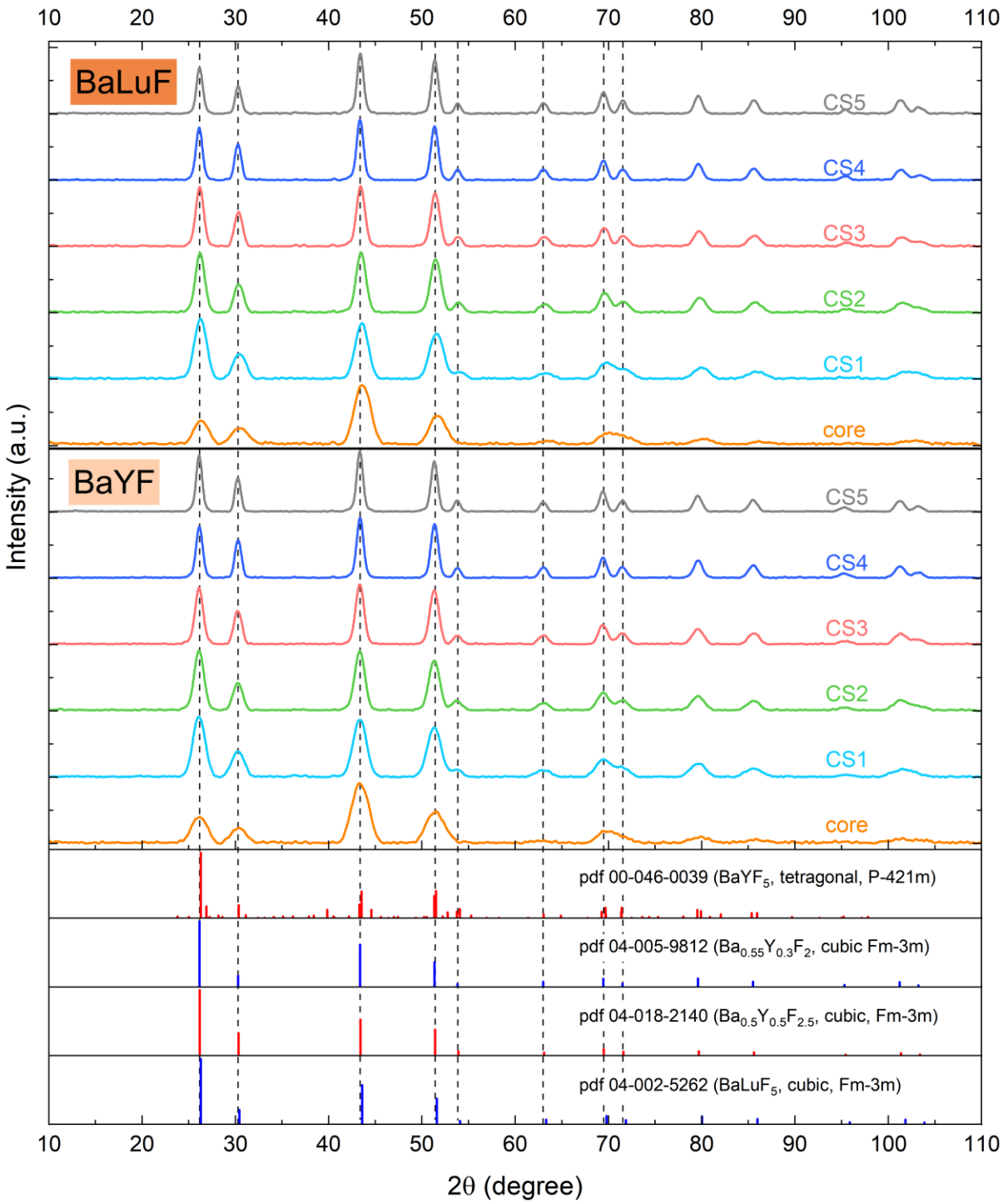

Figure S5. XRD patterns of BaYF and BaLuF samples. Due to the small size of the UCNPs the XRD peaks are broadened. The XRD peaks become sharper with increasing size due to increasing shell thickness. For a large range of stochiometric ratios, the XRD patterns are almost identical for same crystal structure and phase group as shown by different reference powder XRD pattern (pdf). Dashed lines are centered at the peak positions of CS5.

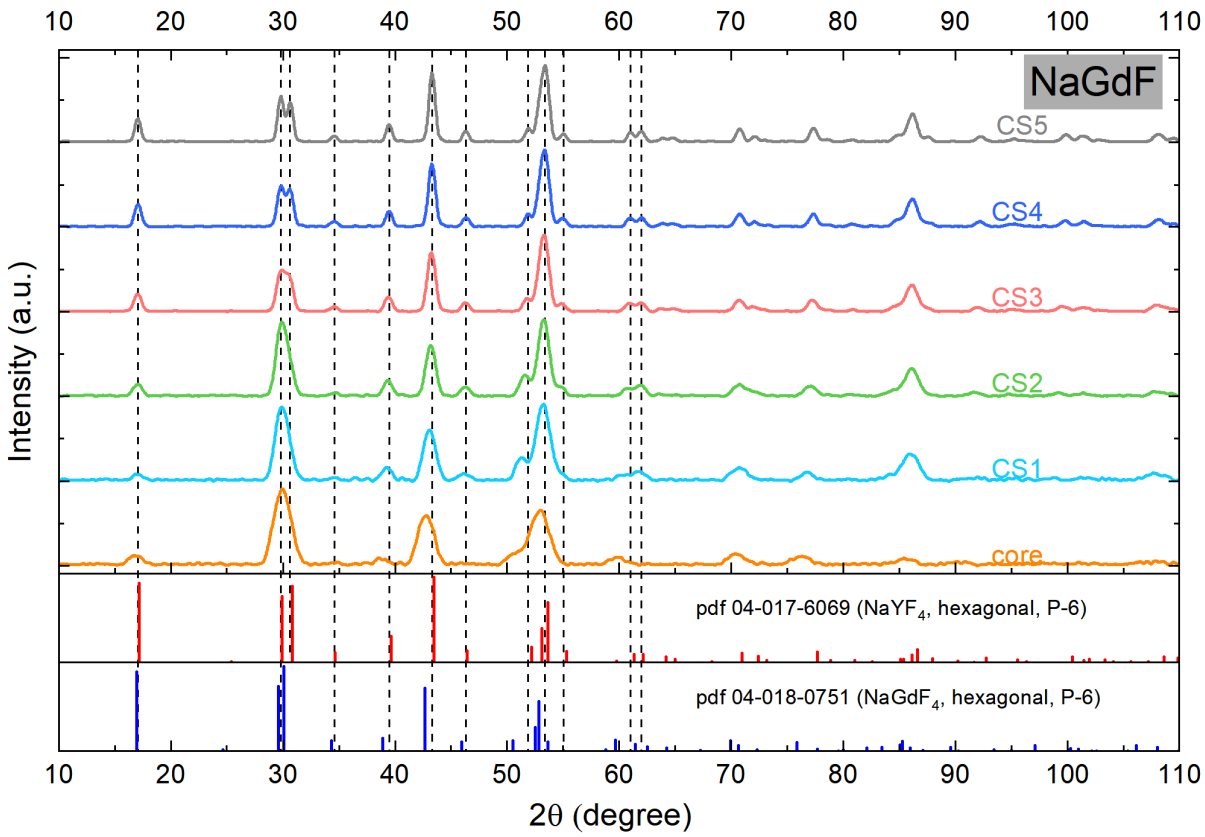

Figure S6. XRD patterns of the reference β-$NaGdF_4$ core and core/shell samples with β-$NaYF_4$ inert shells. All samples are purely hexagonal-phase. Dashed lines are centered at the peak positions of CS5.

2.2 TEM images

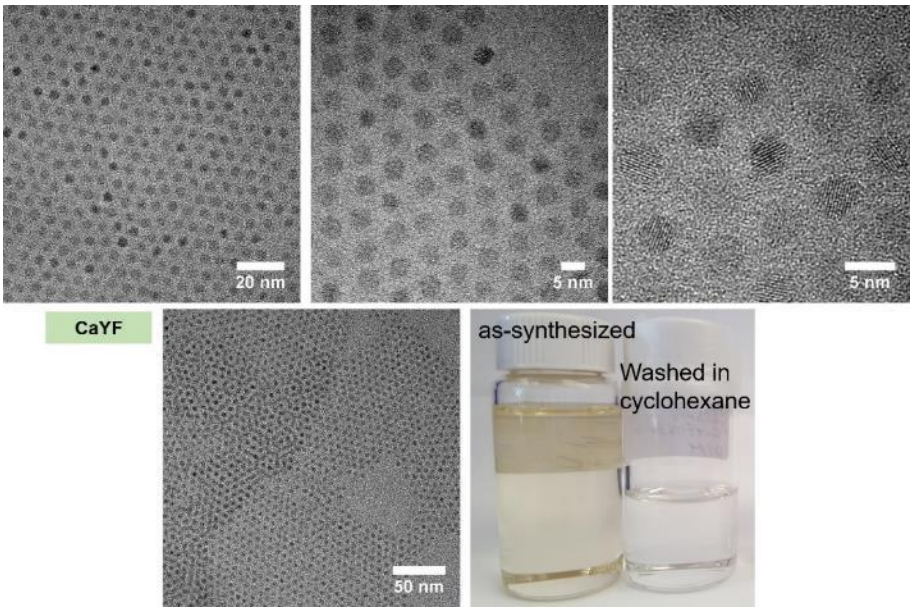

Figure S7. TEM images of the CaYF core UCNPs at different magnifications. Photograph of the as-synthesized UCNPs and the washed UCNPs in cyclohexane.

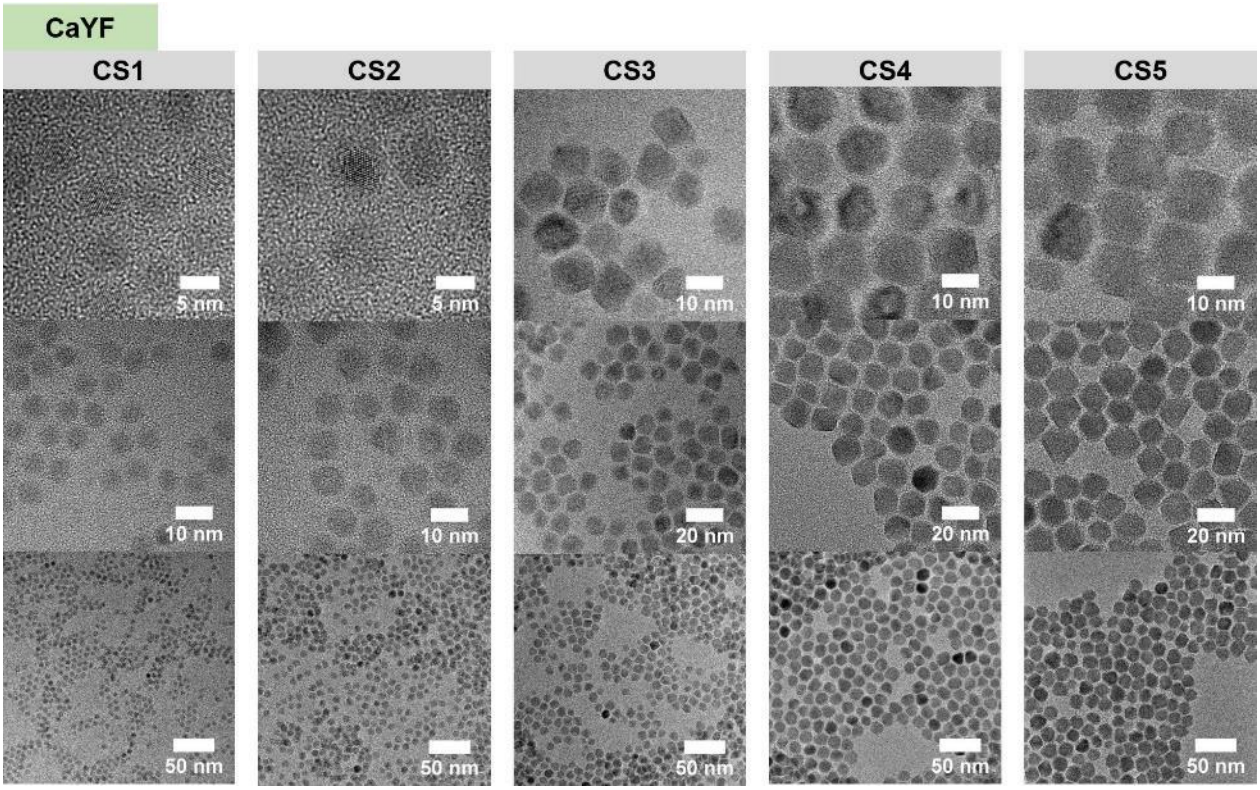

Figure S8. TEM images of the core/shell CaYF UCNCs with inert CaYF shell layers at different magnifications.

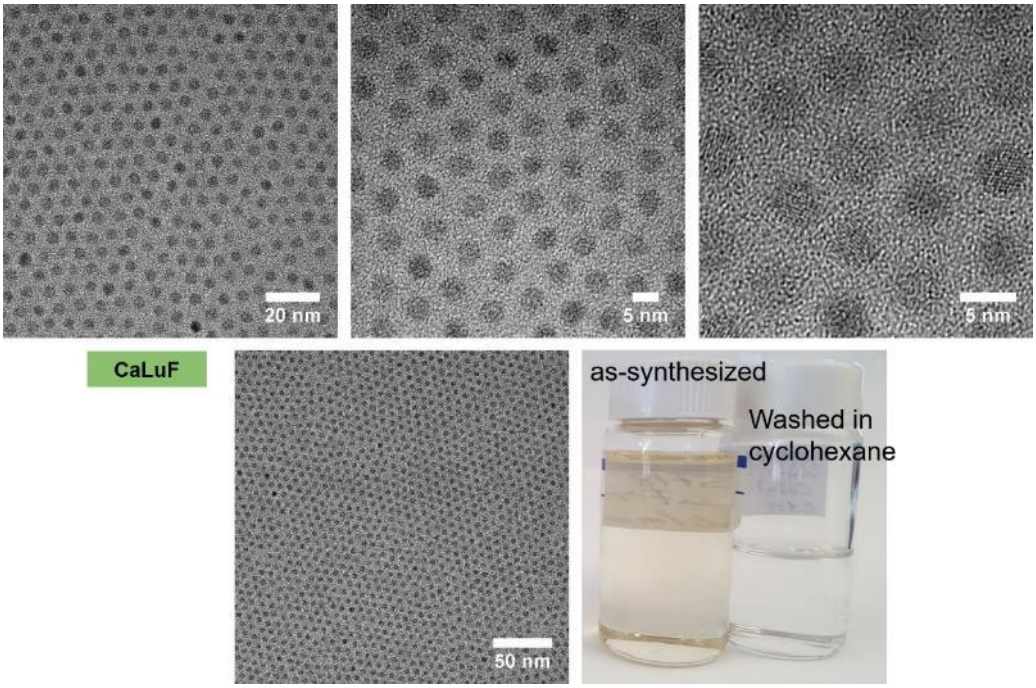

Figure S9. TEM images of the CaLuF core UCNPs at different magnifications. Photograph of the as-synthesized UCNPs and the washed UCNPs in cyclohexane.

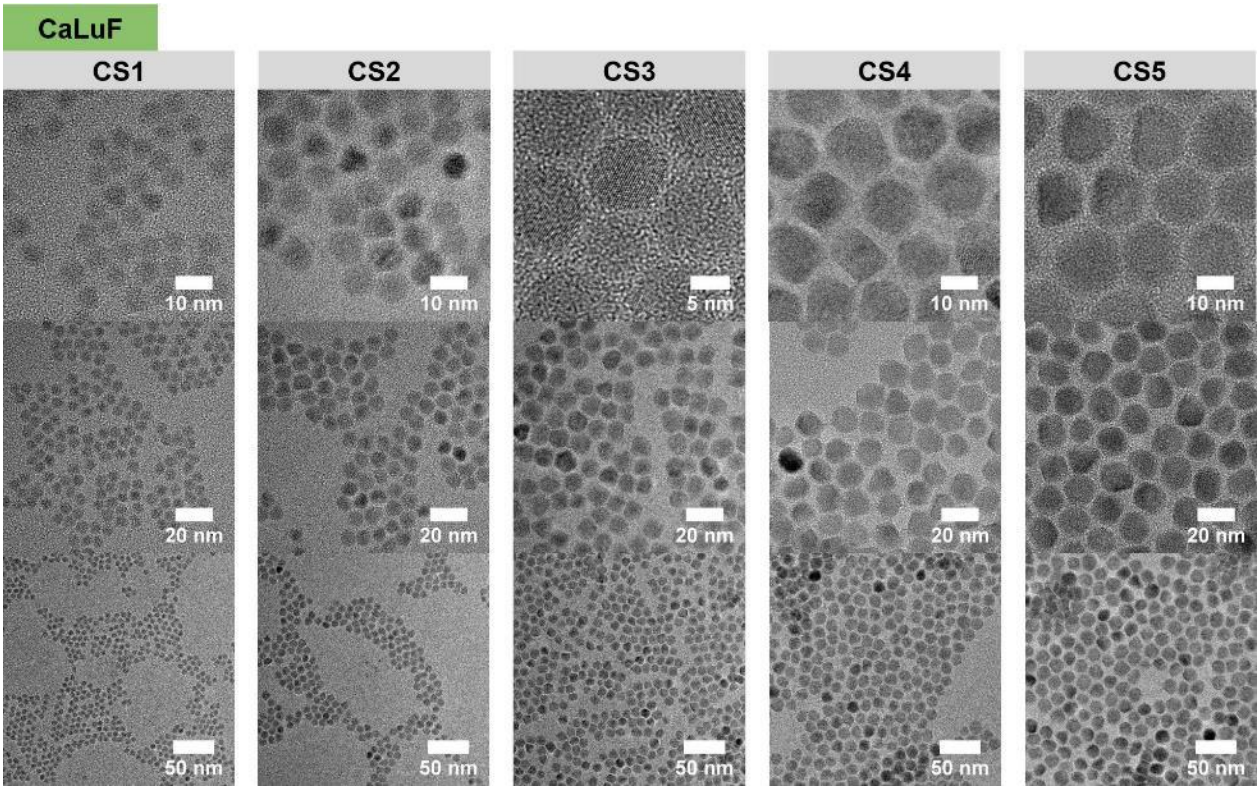

Figure S10. TEM images of the core/shell CaLuF UCNCs with inert CaYF shell layers at different magnifications.

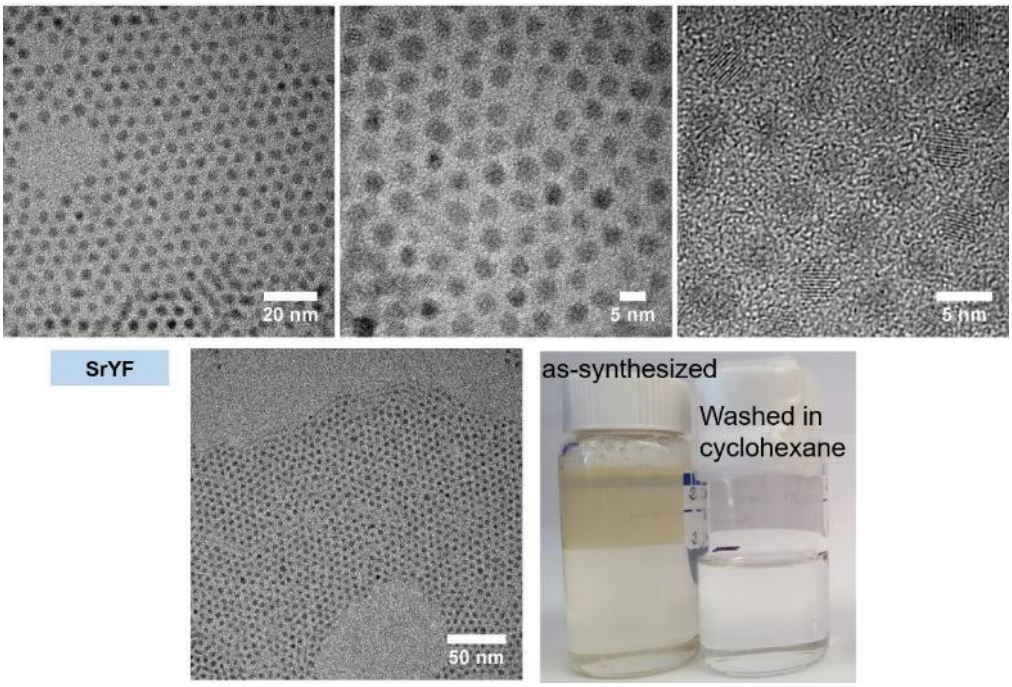

Figure S11. TEM images of the SrYF core UCNPs at different magnifications. Photograph of the as-synthesized UCNPs and the washed UCNPs in cyclohexane.

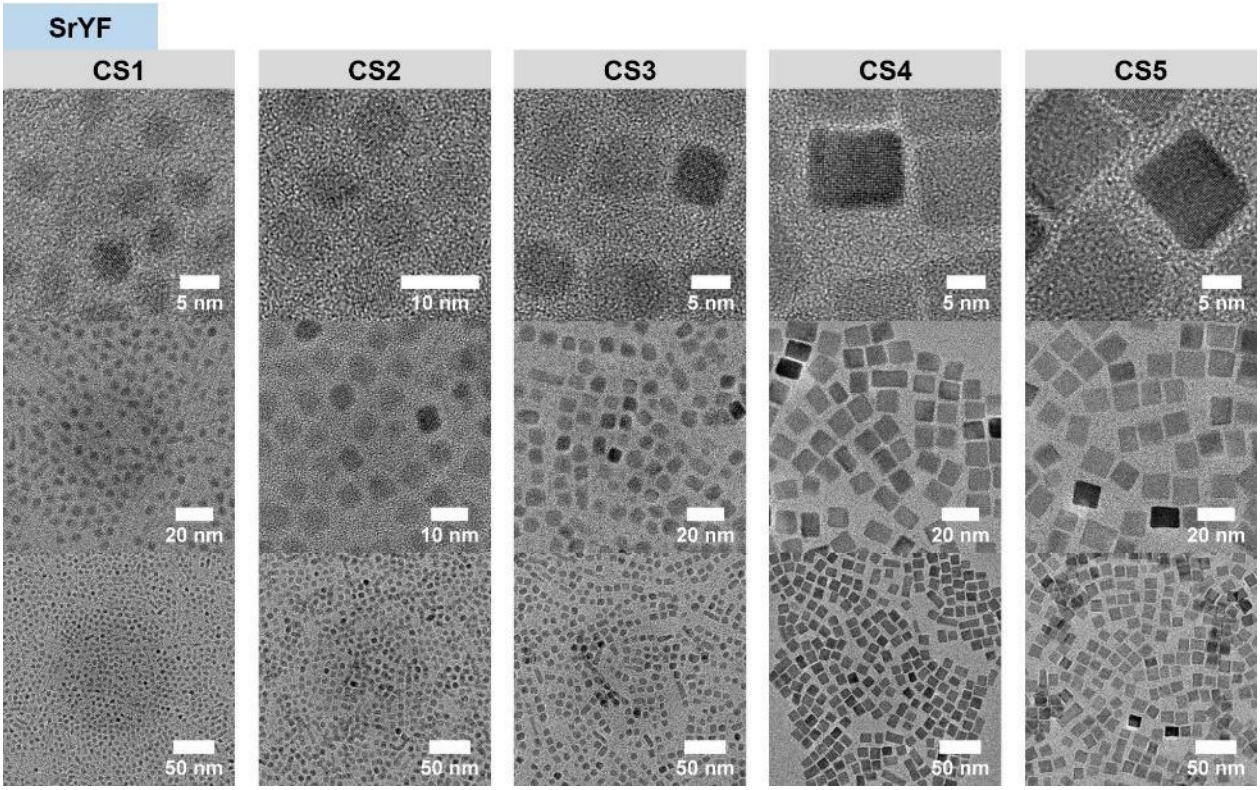

Figure S12. TEM images of the core/shell SrYF UCNCs with inert SrYF shell layers at different magnifications.

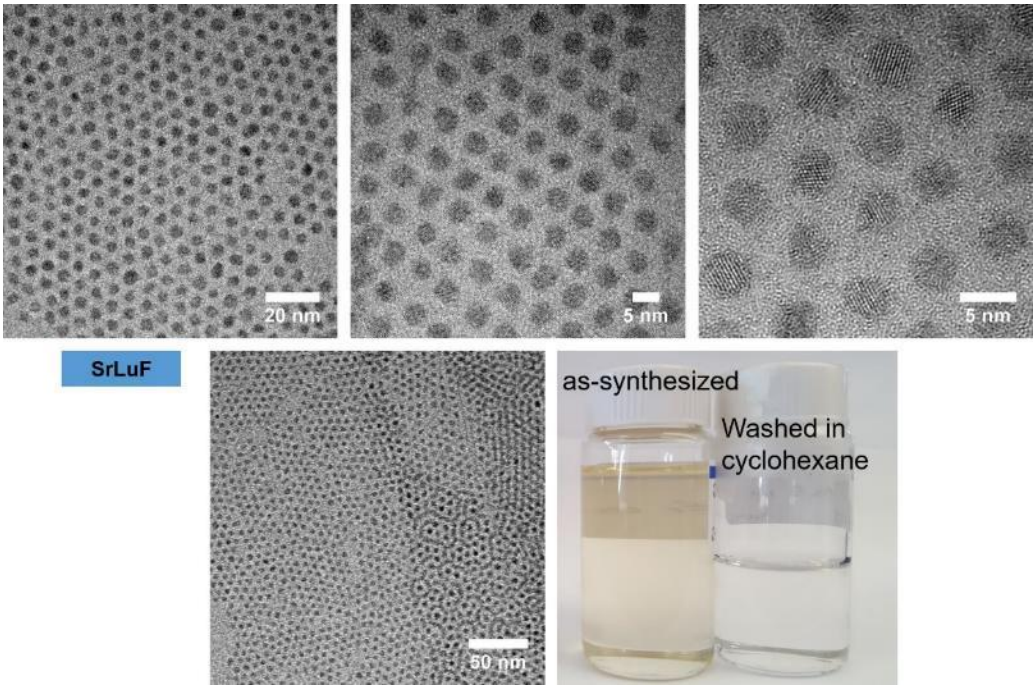

Figure S13. TEM images of the SrLuF core UCNPs at different magnifications. Photograph of the as-synthesized UCNPs and the washed UCNPs in cyclohexane.

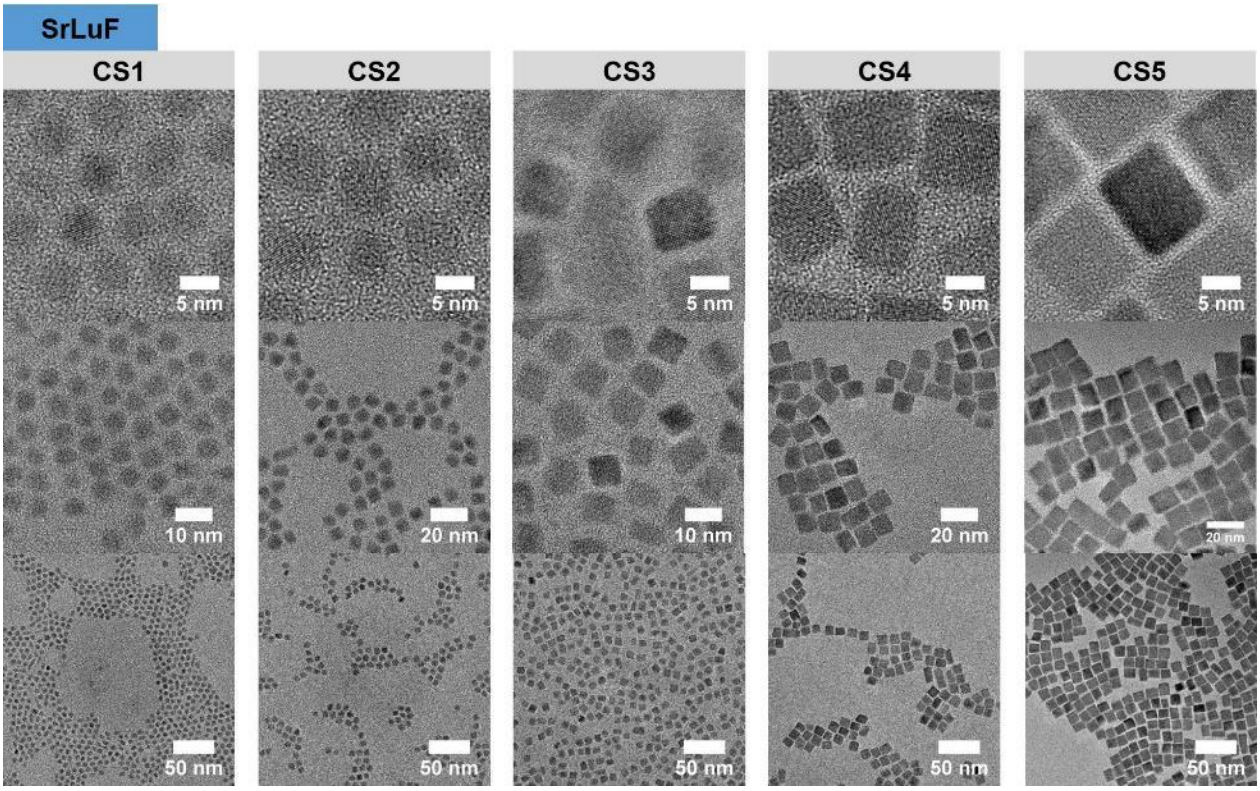

Figure S14. TEM images of the core/shell SrLuF UCNCs with inert SrYF shell layers at different magnifications.

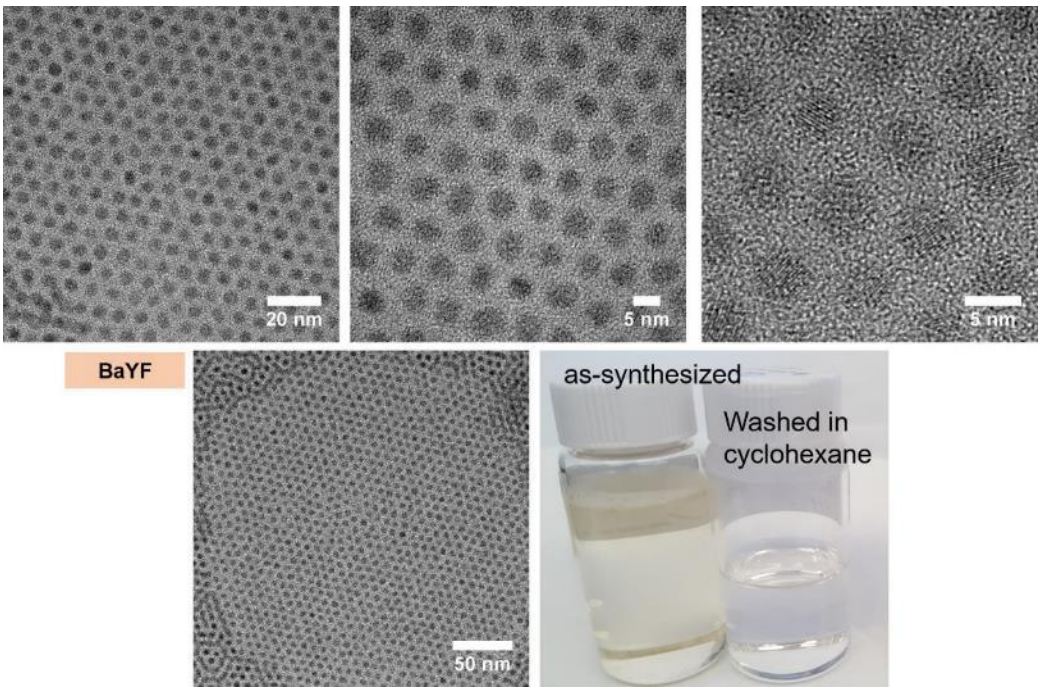

Figure S15. TEM images of the BaYF core UCNPs at different magnifications. Photograph of the as-synthesized UCNPs and the washed UCNPs in cyclohexane.

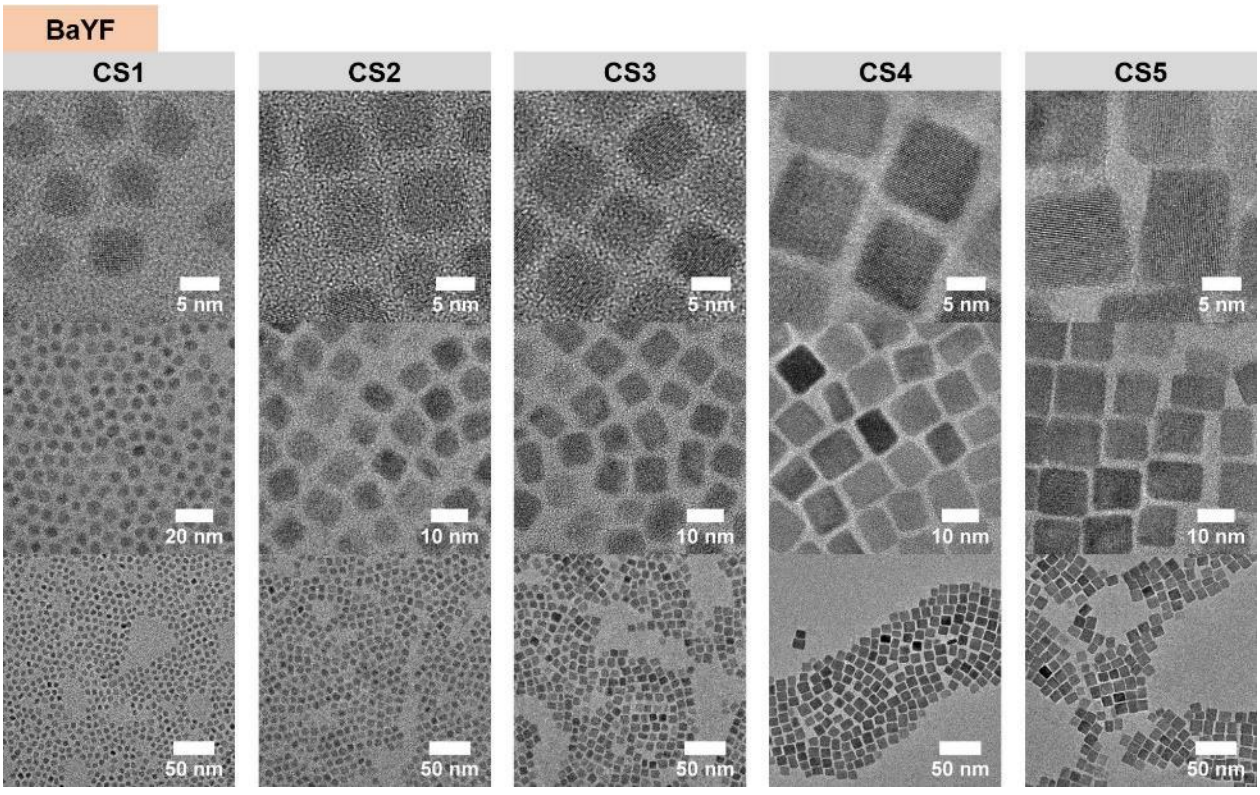

Figure S16. TEM images of the core/shell BaYF UCNCs with inert BaYF shell layers at different magnifications.

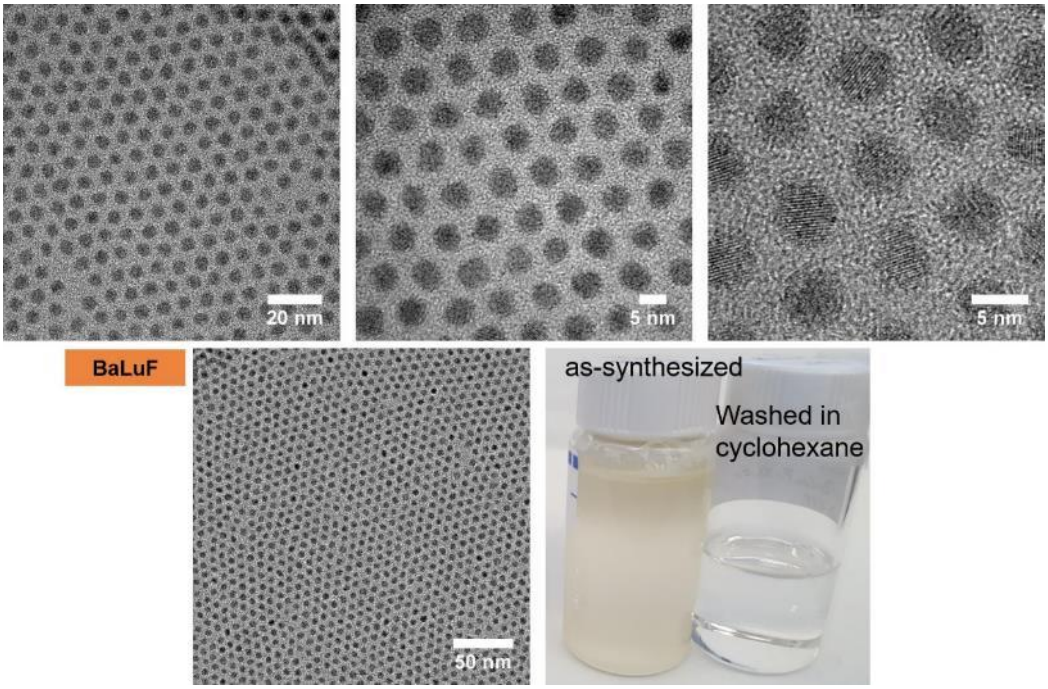

Figure S17. TEM images of the BaLuF core UCNPs at different magnifications. Photograph of the as-synthesized UCNPs and the washed UCNPs in cyclohexane.

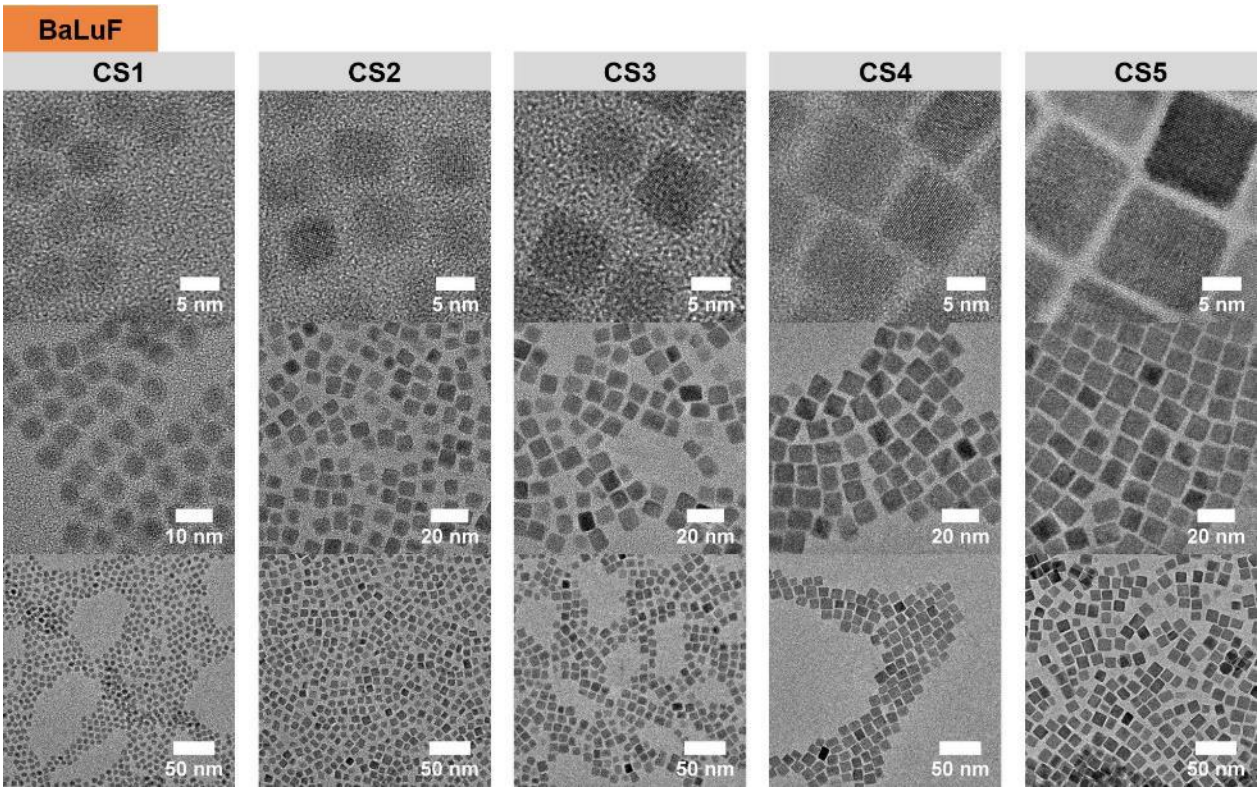

Figure S18. TEM images of the core/shell BaLuF UCNCs with inert BaYF shell layers at different magnifications.

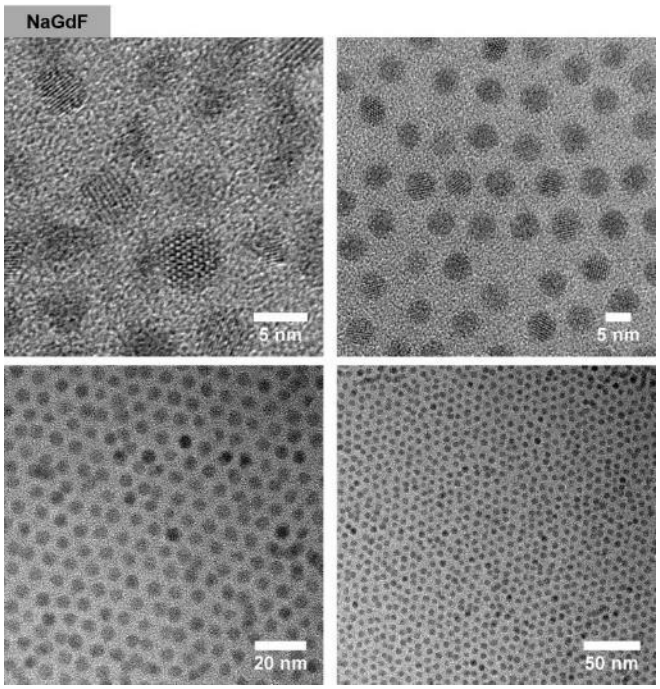

Figure S19. TEM images of the β-$NaGdF_4$ core UCNPs at different magnifications. Photograph of the as-synthesized UCNPs and the washed UCNPs in cyclohexane.

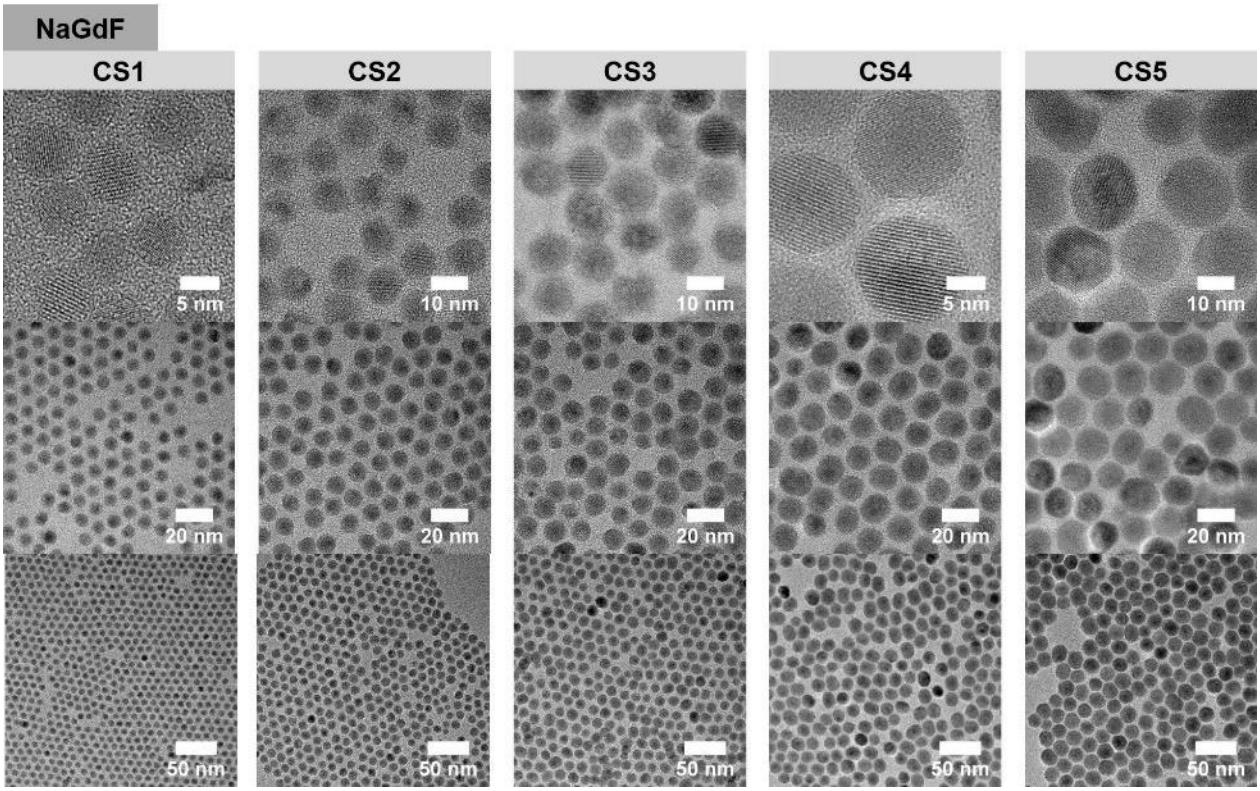

Figure S20. TEM images of the core/shell β-$NaGdF_4$ UCNCs with inert β-$NaYF_4$ shell layers at different magnifications.

2.3 Size distribution by TEM analysis

The size distributions were determined from measuring the projected area of individual nanoparticles in TEM images. We measured the area of at least 300 nanoparticles for each sample and calculated the diameter of spherical particles and the edge length of cubic particles. In order to compare spherical and cubic particles and to define a shell thickness, we converted the area of cubic particles, which are all MLnF UCNCs from CS2 to CS5, into an estimated diameter, whereas the volume of the sphere equals the volume of a cube ($V_{cube} = V_{sphere}$) using Equation S1 and Equation S2.

$$V_{cube} = a^3 = A_{cube}^{3/2} \qquad V_{sphere} = \frac{4}{3}\pi r^3 \tag{S1}$$

$$V_{cube} = V_{sphere} \rightarrow r^* = \sqrt[3]{\frac{3}{4\pi} A_{cube}^{3/2}} = \sqrt[3]{\frac{3}{4\pi}} \sqrt{A_{cube}} \approx 0.62\sqrt{A_{cube}} \tag{S2}$$

Finally, we calculated the mean values and standard derivations. The shell thickness in our study is derived from the mean values of estimated diameters.

Table S3. Edge length and diameter of all nanoparticles in this study as measured by TEM analysis using the projected area of the particles. The estimated diameters are converted as outlined in the text and used throughout the study including the calculation of the shell thickness. Values marked with # are treated as spheres.

Edge length or diameter calculated from area (nm) (#treated as sphere)							
	CaYF	**CaLuF**	**SrYF**	**SrLuF**	**BaYF**	**BaLuF**	**NaGdF**
core	4.6±0.5#	4.8±0.3#	4.5±0.4#	4.9±0.4#	5.2±0.4#	5.7±0.4#	5.4±0.6#
CS1	6.2±0.6#	6.0±0.6#	5.5±0.6#	6.1±0.7#	6.7±0.6#	6.4±0.6#	7.3±0.4#
CS2	6.7±0.9	6.8±0.7	6.0±0.7	6.4±0.6	7.2±0.7	7.5±0.8	9.6±0.7#
CS3	8.2±1.2	8.6±0.9	7.1±0.8	7.9±0.7	8.2±0.9	8.5±1.0	11.7±1.6#
CS4	11.7±1.2	11.5±1.2	10.5±1.0	9.6±0.9	10.2±1.2	10.6±1.2	15.3±2.1#
CS5	14.0±1.8	14.4±1.5	12.4±1.7	11.0±1.0	11.6±1.2	11.7±1.5	17.7±1.9#
Estimated diameter by converting cube to sphere as outlined in the text (nm)							
	CaYF	**CaLuF**	**SrYF**	**SrLuF**	**BaYF**	**BaLuF**	**NaGdF**
core	4.6±0.5	4.8±0.3	4.5±0.4	4.9±0.4	5.2±0.4	5.7±0.4	5.4±0.6
CS1	6.2±0.6	6.0±0.6	5.5±0.6	6.1±0.7	6.8±0.6	6.4±0.6	7.3±0.4
CS2	8.3±1.1	8.4±0.9	7.4±0.9	7.9±0.8	9.0±0.9	9.3±1.0	9.6±0.7
CS3	10.2±1.5	10.7±1.1	8.8±1.0	9.8±0.9	10.2±1.1	10.6±1.3	11.7±1.6
CS4	14.5±1.5	14.3±1.5	13.0±1.2	11.9±1.2	12.6±1.5	13.2±1.5	15.3±2.1
CS5	17.5±2.3	17.8±1.8	15.4±2.1	13.6±1.2	14.4±1.5	14.5±1.9	17.7±1.9
Shell thickness based on estimated diameter (nm)							
	CaYF	**CaLuF**	**SrYF**	**SrLuF**	**BaYF**	**BaLuF**	**NaGdF**
core							
CS1	0.8±0.4	0.6±0.4	0.5±0.4	0.6±0.4	0.8±0.4	0.3±0.3	1.0±0.4
CS2	1.9±0.6	1.8±0.5	1.5±0.5	1.5±0.4	1.9±0.5	1.8±0.6	2.1±0.5
CS3	2.8±0.8	2.9±0.6	2.1±0.5	2.5±0.5	2.5±0.6	2.5±0.6	3.2±0.9
CS4	4.9±0.8	4.7±0.8	4.2±0.6	3.5±0.6	3.7±0.8	3.8±0.8	5.0±1.1
CS5	6.4±1.2	6.5±0.9	5.4±1.1	4.4±0.6	4.6±0.8	4.4±0.9	6.2±1.2

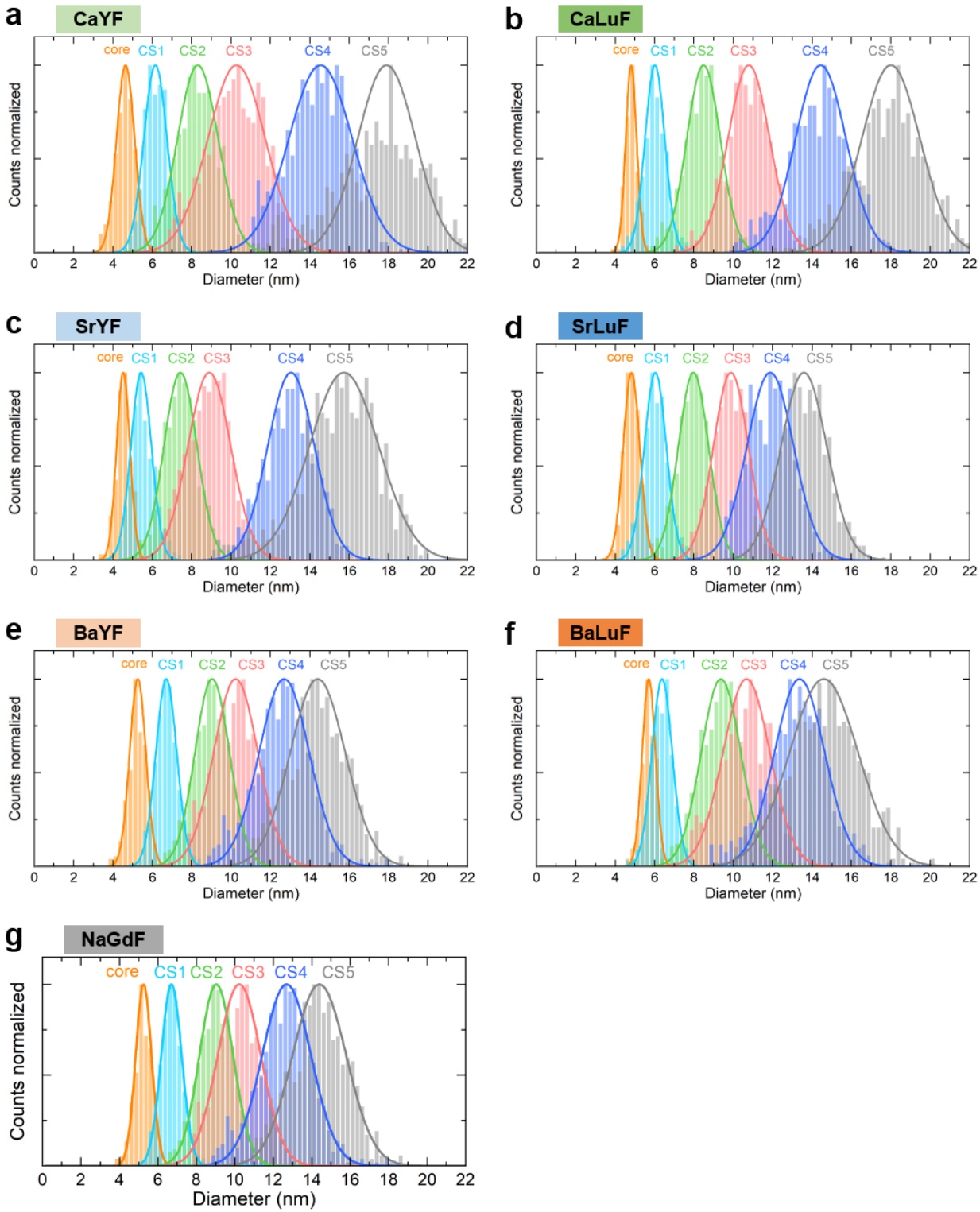

Figure 21S. Size distribution of core and core/shell UCNCs of a) CaYF, b) CaLuF, c) SrYF, d) SrLuF, e) BaYF, f) BaLuF, and g) β-$NaGdF_4$. Here, the distribution of estimated diameters for all samples are shown. The distributions are normalized to the maximum count value and the solid lines represent Gaussian fits.

3 Optical characterization and methods

Detailed descriptions of the experimental setups can be found in previous works.[4]

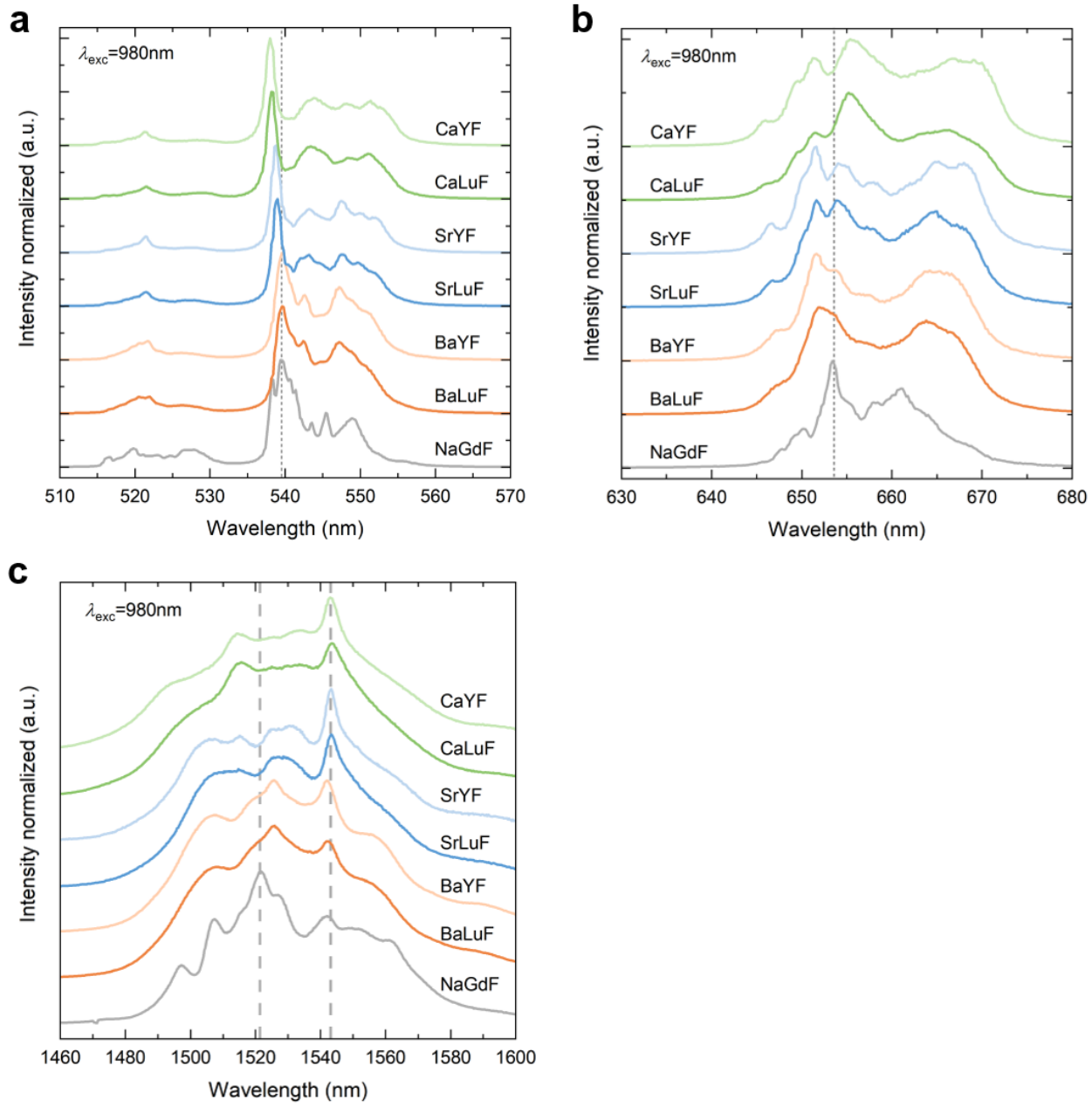

Figure S22. Emission spectra under 980 nm cw laser excitation for Er^{3+} transitions of a) green ($^2H_{11/2}$, $^4S_{3/2}$)→$^4I_{15/2}$, b) red $^4F_{9/2}$→$^4I_{15/2}$ Er^{3+}, and c) NIR $^4I_{13/2}$→$^4I_{15/2}$.

3.1 Absorption correction for UCQY measurements

We used an integrating sphere for upconversion quantum yield (UCQY) measurements. In UCQY measurements the absorptance of the sample is determined by measuring the excitation spectrum from a source, a 980 nm cw laser in our case, with a reference and the sample. The reference should have the same properties as the sample without the absorption. Usually, the reference is the solvent or un-doped nanoparticles of similar size to mimic the scattering. The amount of absorbed light by the sample is the difference between reference and sample.

We measured an offset signal in the NIR spectra around the laser wavelength due to emission from the UCNP samples from Er^{3+} $^4I_{11/2} \rightarrow {}^4I_{15/2}$ and Yb^{3+} $^2F_{5/2} \rightarrow {}^2F_{7/2}$ transitions (see Figure S23a). This emission is parasitic for the UCQY calculations as it results in an underestimation of the samples' absorptance. This manifests in an increasing UCQY value (decreasing absorptance) for larger integration ranges around the 980 nm laser excitation (Figure S23b). To eliminated this effect, we measured the emission spectrum of the samples under direct excitation of the sample around 980 nm by using two different laser excitation wavelengths, 965 nm and 985 nm. We used an excitation of 965 nm to measure the shorter wavelength part from 900 to 980 nm and an excitation of 985 nm to collect the longer wavelength part from 970 to 1100 nm. The two spectra are stitched to result in the emission spectra shown in Figure S24b. These spectra were then used to subtract the background emission in the NIR spectra from Figure S22a by fitting the 980 nm emission spectra in the ranges from 940 to 970 nm and 990 to 1130 nm. By applying this correction, the measured absorptance of the samples increase, which results in lower UCQY values. Importantly, using this correction the UCQY values do no longer depend on the integration range used for the UCQY calculation as shown in Figure S25. We applied the absorptance correction to all samples and UCQY measurements in this work.

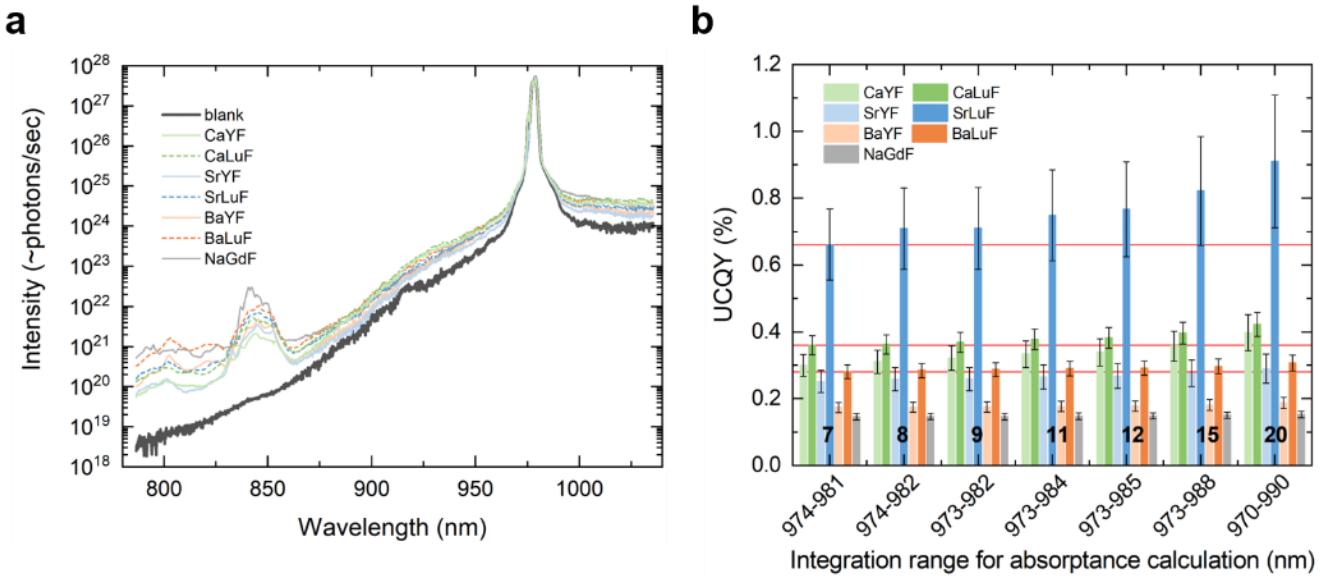

Figure S23. a) Representative calibrated NIR spectrum of the 980 nm laser excitation for UCQY measurements via an integrating sphere with blank and CS5 samples loaded to calculate the absorptance of the samples. Parasitic emission for the UCQY calculation from Yb^{3+} $^2F_{5/2}\rightarrow{}^2F_{7/2}$ and Er^{3+} $^4I_{11/2}\rightarrow{}^4I_{15/2}$ transition overlap with the laser profile leading to underestimation of the samples' absorptance. The broad parasitic emission is apparent from the higher signal for all samples compared to the blank sample. b) This parasitic emission manifests in absorptance values that depend on the used integration range for the calculation of the absorptance. The wider the absorption range, as indicated by the bold numbers in the bar plot, the lower the calculated absorptance and consequently higher the UCQY values. This effect is more or less strongly pronounced for the different samples but all samples show this dependence. We addressed this issue by subtracting the parasitic emission which results in generally lower UCQY values reported in this study.

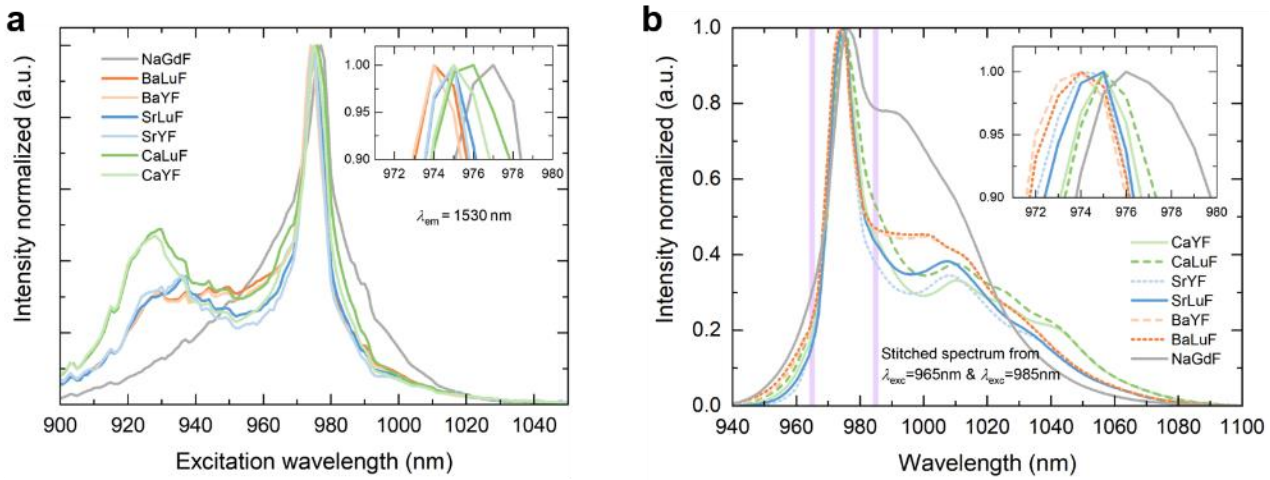

Figure S24. a) Excitation spectra of the Yb^{3+} $^2F_{7/2}\rightarrow{}^2F_{5/2}$ and Er^{3+} $^4I_{15/2}\rightarrow{}^4I_{11/2}$ transition for emission of the Er^{3+} $^4I_{13/2}\rightarrow{}^4I_{15/2}$ transition around 1500 nm for CS5 samples. The peak in the spectra for all MLnF samples shift to shorter wavelengths compared to the NaGdF sample. In contrast to NaGdF, all MLnF samples show emission around 1500 nm when excited around 920-940 nm. b) Emission spectra of Yb^{3+} $^2F_{5/2}\rightarrow{}^2F_{7/2}$ and Er^{3+} $^4I_{11/2}\rightarrow{}^4I_{15/2}$ transition when excited directly. The samples are excited at 965 nm to collect the longer wavelength part from 970 to 1100 nm and at 985 nm to measure the shorter wavelength part from 900 to 980 nm. The two spectra are stitched to result in the shown emission spectra that was used to correct the NIR spectra in UCQY measurements for parasitic emission. As in the excitation spectra, the peaks in the spectra shifts towards shorter wavelengths for heavier alkaline-earth metals.

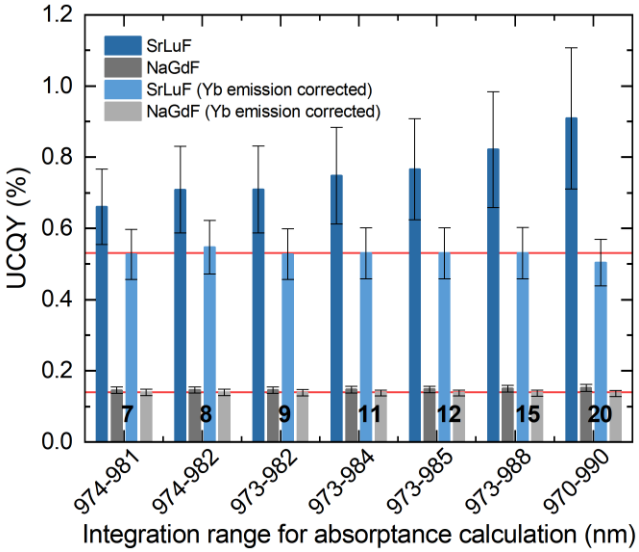

Figure S25. Comparison of UCQY values with and without correction of emission from Yb^{3+} $^2F_{5/2}\rightarrow{}^2F_{7/2}$ and Er^{3+} $^4I_{11/2}\rightarrow{}^4I_{15/2}$. We subtracted the 980 nm emission spectrum of the different compounds by fitting the 980 nm emission spectra to the background signal in all NIR spectra (Figure S23a) and subtracting it from the NIR spectra for the absorptance calculations. The corrected UCQY values do not depend on the integration range used for the UCQY calculations and are lower than the uncorrected values. Corrected UCQY values are reported throughout this work. We used an integration range from 973 to 982 nm.

3.2 Time-dependent luminescence and upconversion quantum yield measurements

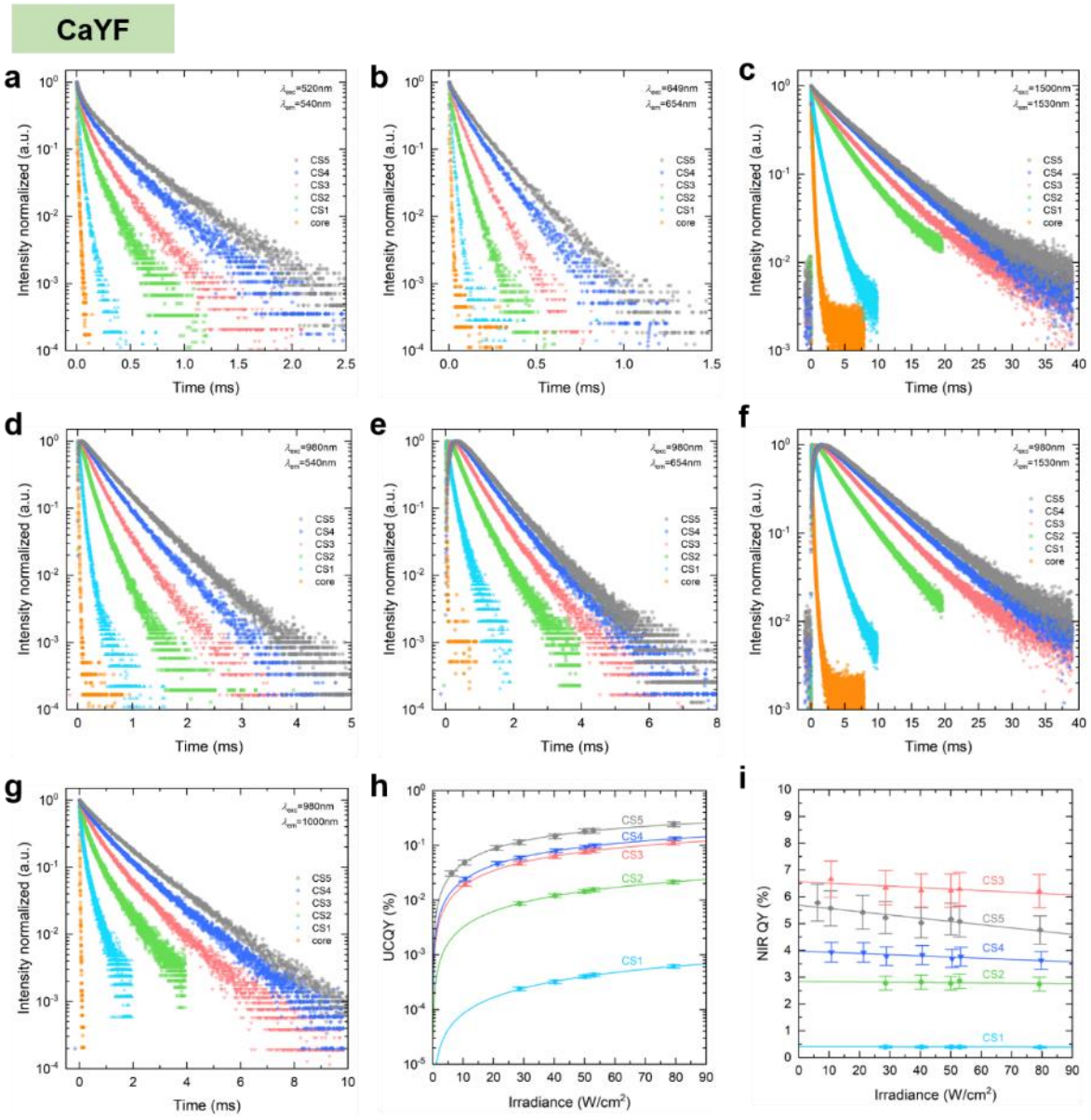

Figure S26. Time-dependent luminescence of CaYF core and core/shell samples of various transitions under direct excitation of the energy level and under 980 nm excitation (UC mode). We monitored time-dependent luminescence of the following transitions: Er^{3+} $^4S_{3/2}\rightarrow{}^4I_{15/2}$ (540 nm, green), Er^{3+} $^4F_{9/2}\rightarrow{}^4I_{15/2}$ (654 nm, red), Yb^{3+} $^2F_{7/2}\rightarrow{}^2F_{5/2}$ (1000 nm, NIR), and Er^{3+} $^4I_{13/2}\rightarrow{}^4I_{15/2}$ (1530 nm, NIR). The excitation and emission wavelengths are a) λ_{exc} = 520 nm, λ_{em} = 540 nm, b) λ_{exc} = 649 nm, λ_{em} = 654 nm, c) λ_{exc} = 1500 nm, λ_{em} = 1530 nm, d) λ_{exc} = 980 nm, λ_{em} = 540 nm, e) λ_{exc} = 980 nm, λ_{em} = 654 nm; f) λ_{exc} = 980 nm, λ_{em} = 1530 nm, and g) λ_{exc} = 980 nm, λ_{em} = 1000 nm. h) UCQY of the core/shell samples as a function of irradiance on a log-scale. The UCQY of the core sample was below the detection limit of ~10^{-5}%. i) The NIR UCQY for 980nm excitation and emission around 1530 nm is fairly constant or decreases slightly with irradiance, as observed and described in previous works for β-$NaLnF_4$ compounds.[3,4]

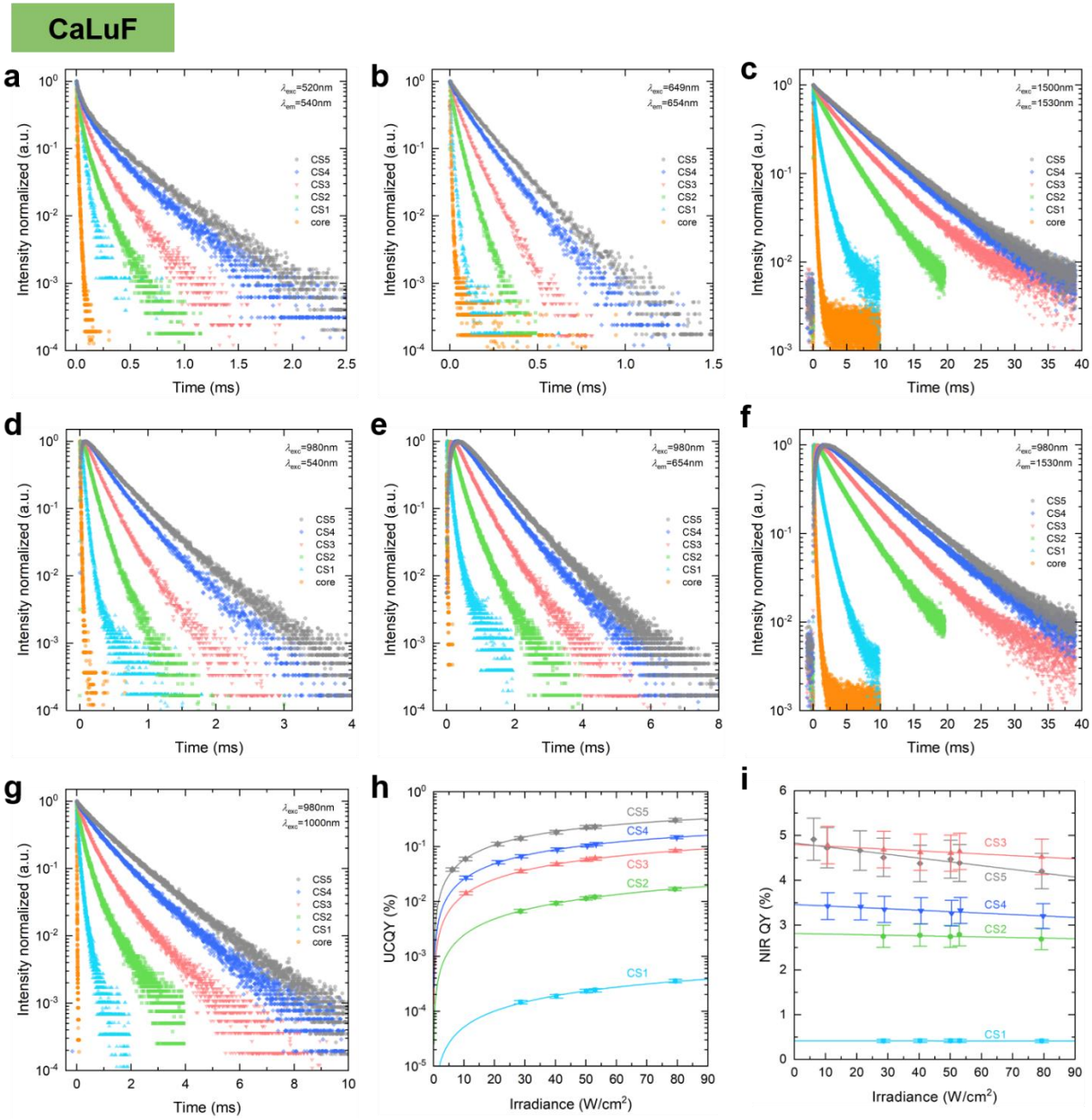

Figure S27. Time-dependent luminescence of CaLuF core and core/shell samples of various transitions under direct excitation of the energy level and under 980 nm excitation (UC mode) and UCQY as a function of irradiance. See caption of Figure S26 for details.

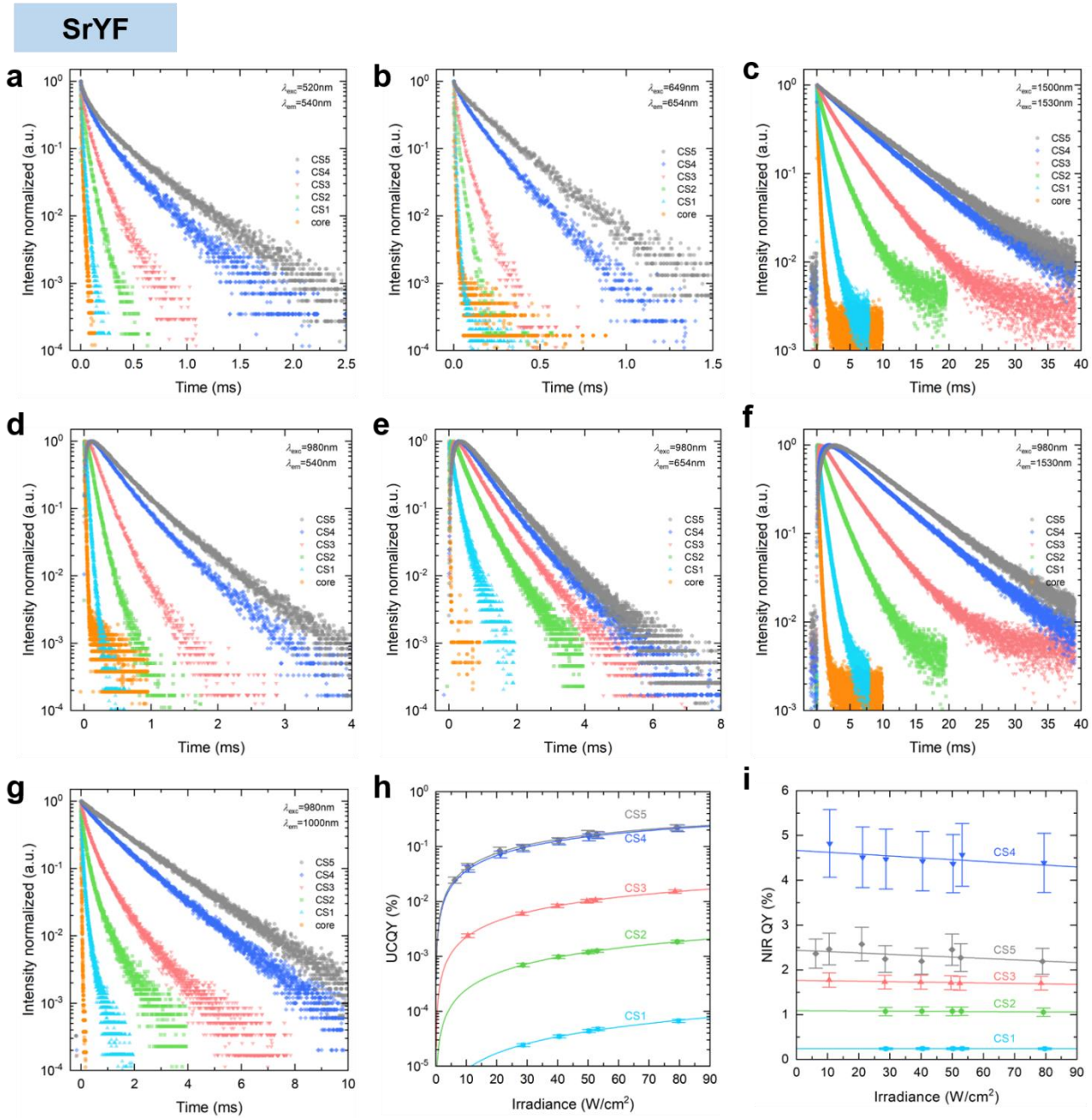

Figure S28. Time-dependent luminescence of SrYF core and core/shell samples of various transitions under direct excitation of the energy level and under 980 nm excitation (UC mode) and UCQY as a function of irradiance. See caption of Figure S26 for details.

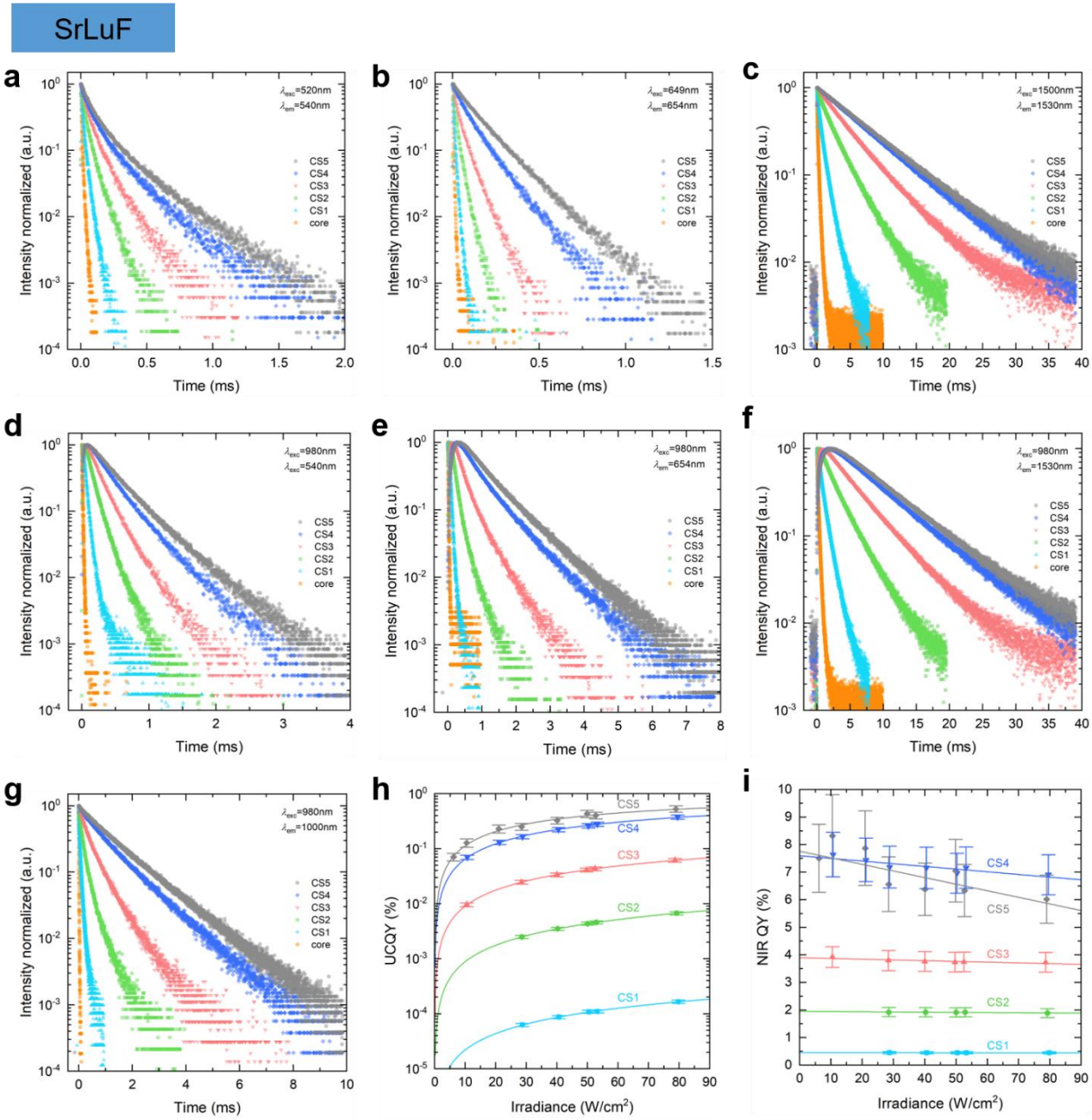

Figure S29. Time-dependent luminescence of SrLuF core and core/shell samples of various transitions under direct excitation of the energy level and under 980 nm excitation (UC mode) and UCQY as a function of irradiance. See caption of Figure S26 for details.

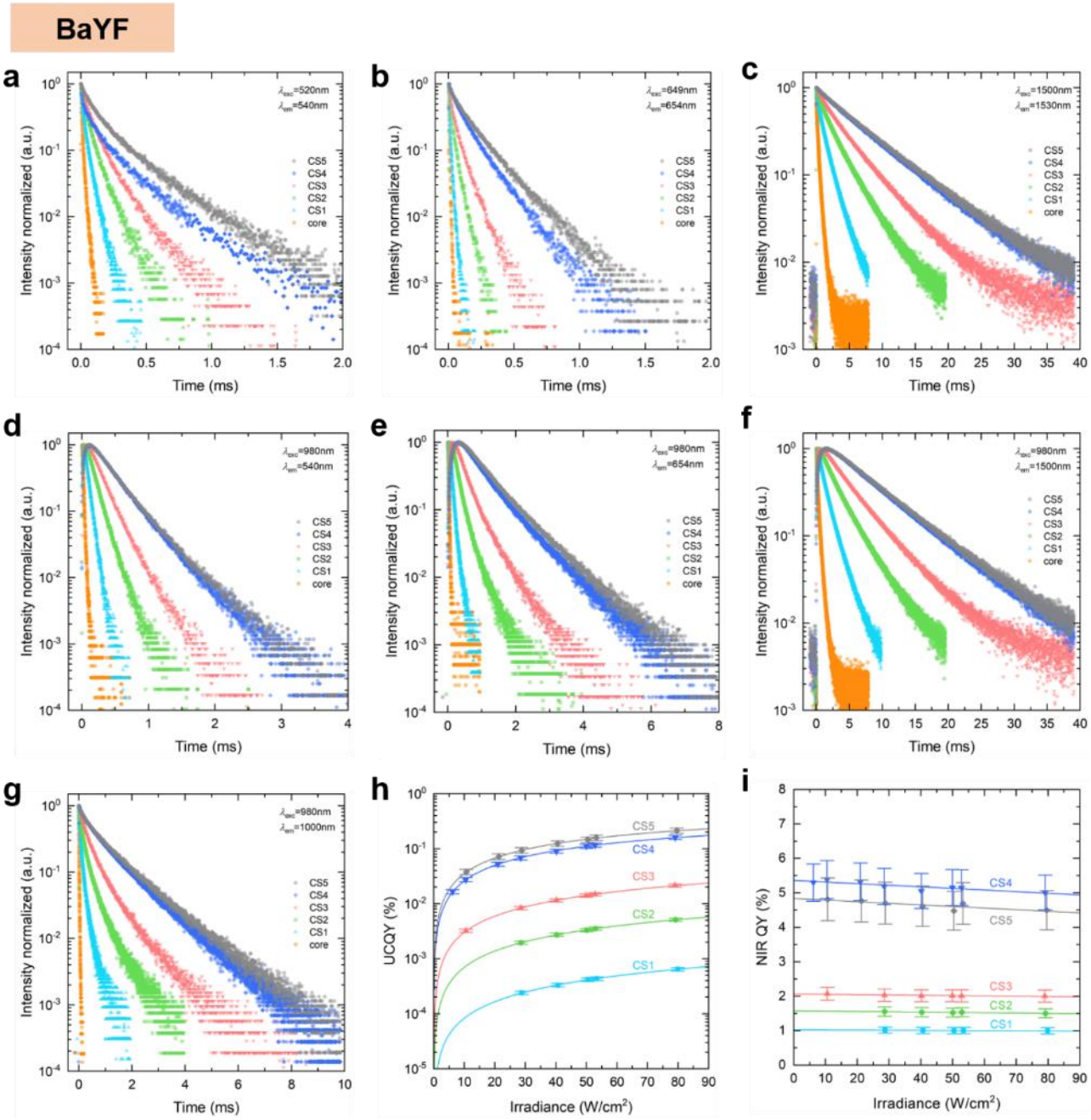

Figure S30. Time-dependent luminescence of BaYF core and core/shell samples of various transitions under direct excitation of the energy level and under 980 nm excitation (UC mode) and UCQY as a function of irradiance. See caption of Figure S26 for details.

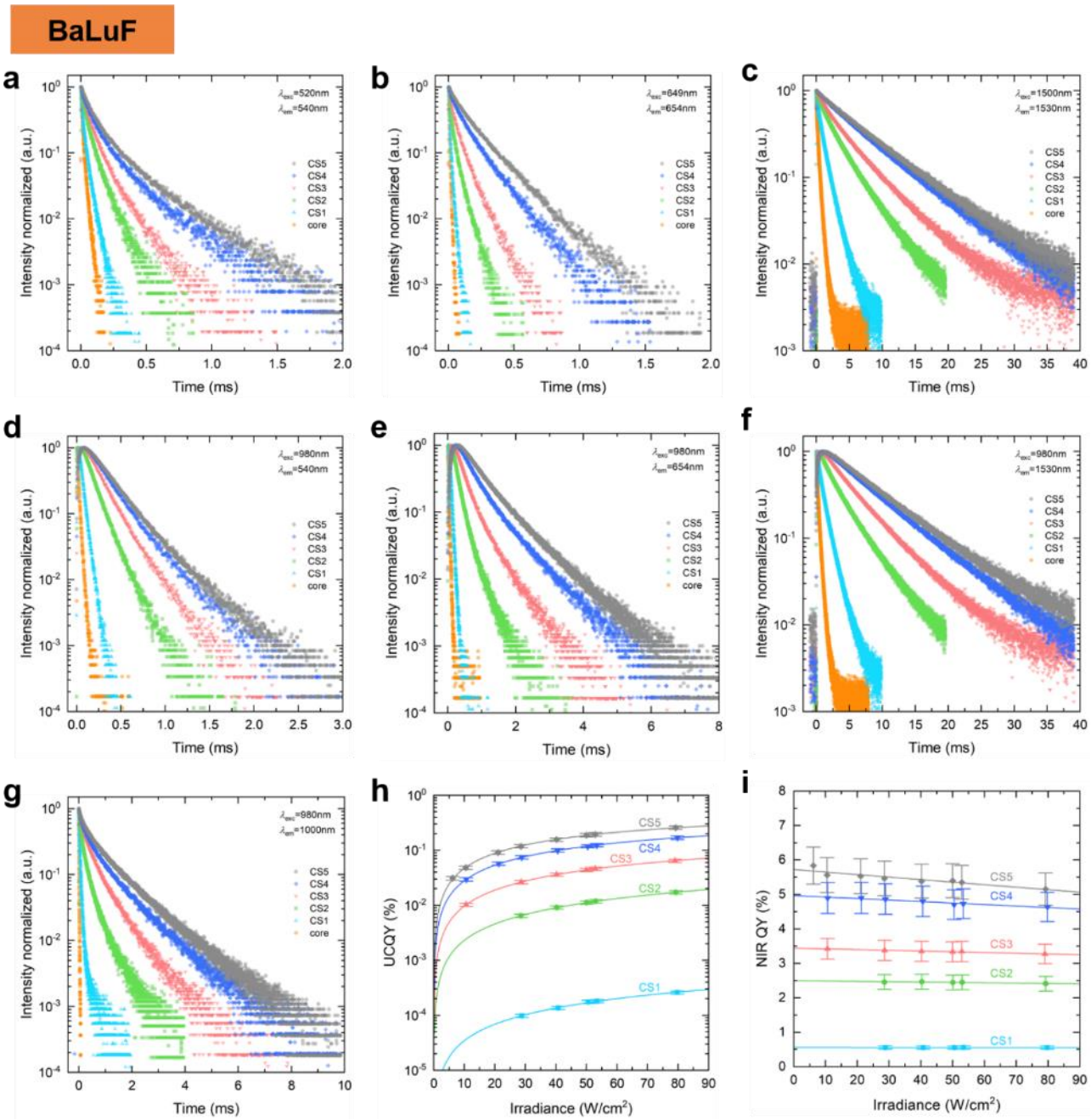

Figure S31. Time-dependent luminescence of BaLuF core and core/shell samples of various transitions under direct excitation of the energy level and under 980 nm excitation (UC mode) and UCQY as a function of irradiance. See caption of Figure S26 for details.

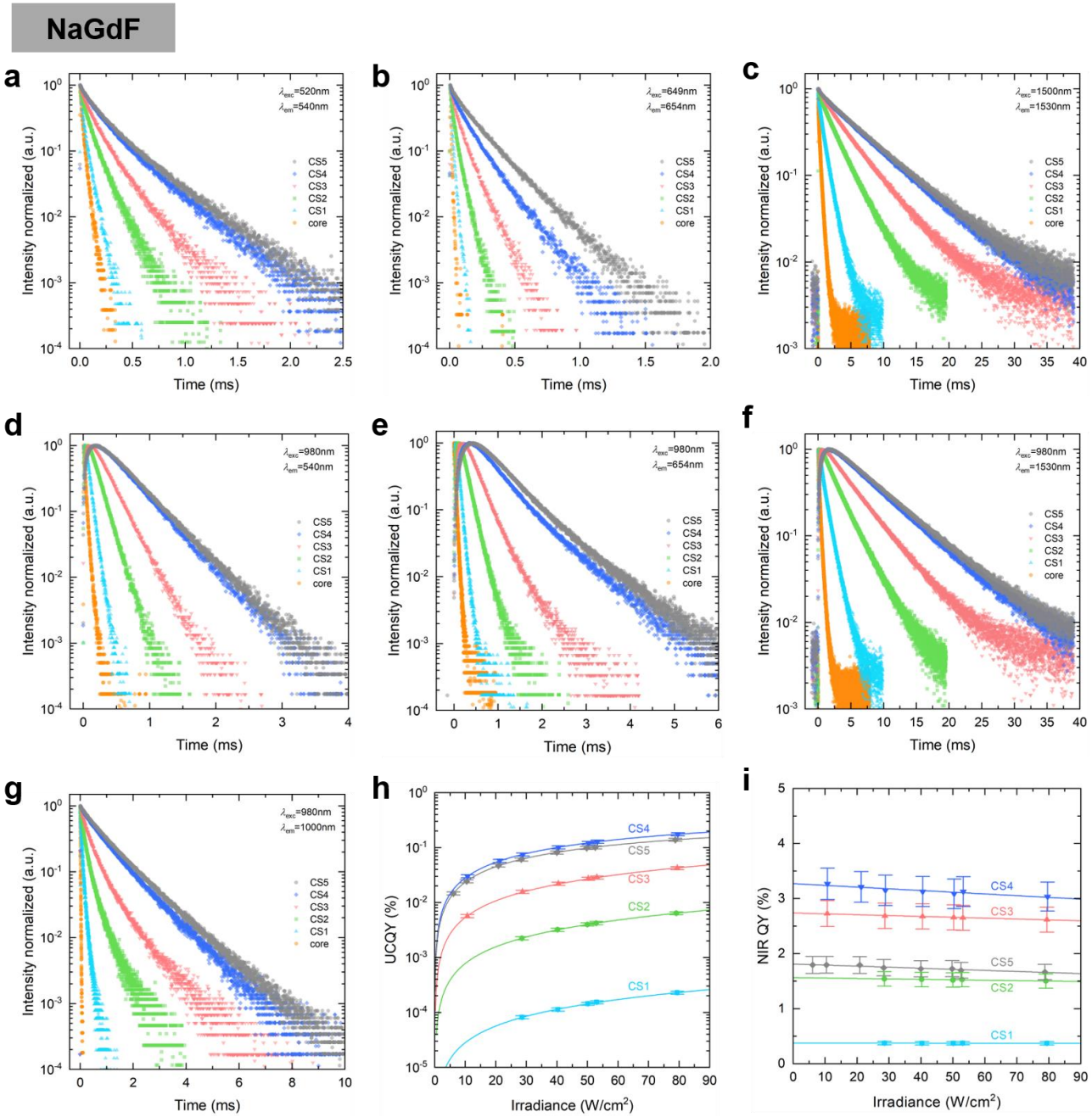

Figure S32. Time-dependent luminescence of CaLuF core and core/shell samples of various transitions under direct excitation of the energy level and under 980 nm excitation (UC mode) and UCQY as a function of irradiance. See caption of Figure S26 for details.

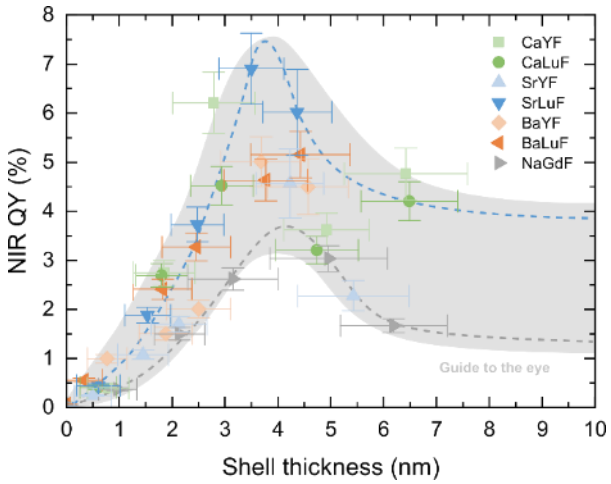

Figure S33. NIR QY for emission around 1500 nm from Er^{3+} $^4I_{13/2}\rightarrow{}^4I_{15/2}$ transition under 980 nm excitation. The NIR QY peaks for a certain shell thickness between 2-5 nm which has been observed and discussed in previous articles.[3,4] The curve of the NIR QY highlights the strong effect of surface quenching on the population of energy levels as well as the dynamics and complexity of the UC processes.

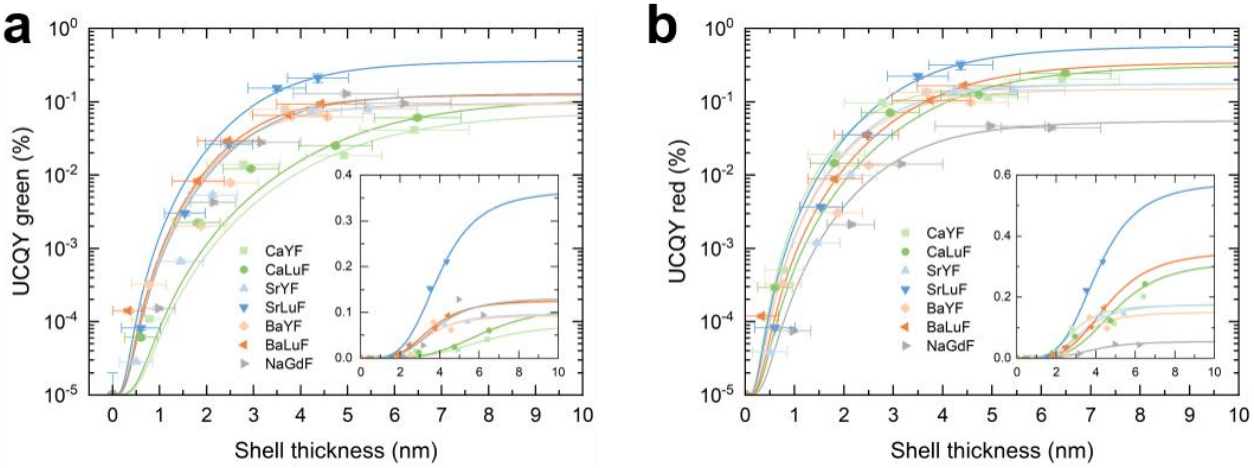

Figure S34. UCQY as a function of the shell thickness on a log-scale y-axis for a) the green emission of the Er^{3+} transition ($^2H_{11/2}$, $^4S_{3/2}$)$\rightarrow{}^4I_{15/2}$ and b) the red emission of Er^{3+} transition $^4F_{9/2}\rightarrow{}^4I_{15/2}$. Insets show the same data with linear y-axis. The data is in good agreement with fits using FRET-type function as described by Equation 1 in the main text.

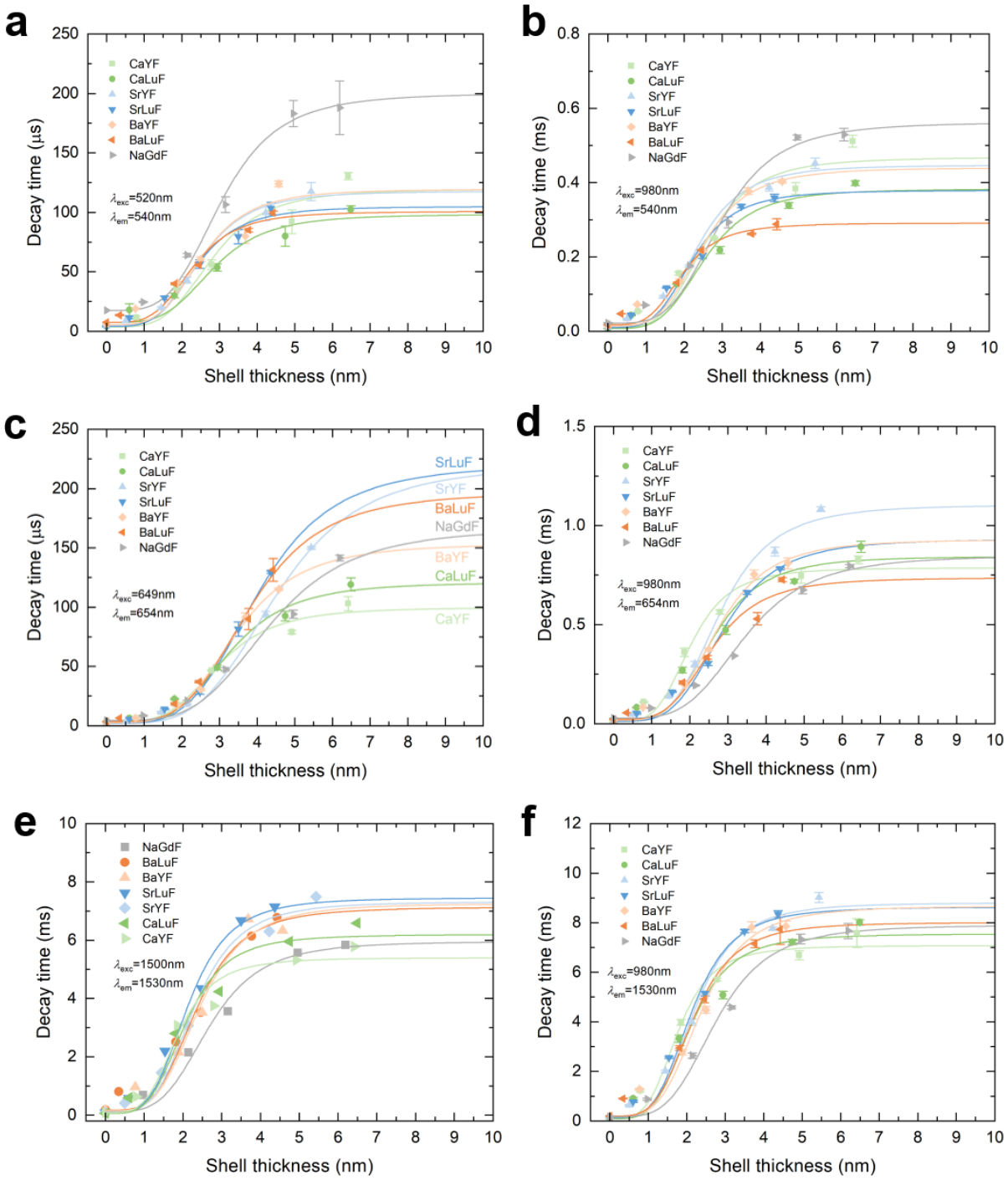

Figure S35. The decay times as a function of shell thickness are in good agreement with fits using a FRET-type function as described in the main text and given by Equation 2 in the main text. The data for the following transitions are given: green emission from Er^{3+} $^4S_{3/2}\rightarrow{}^4I_{15/2}$ using a) direct excitation (λ_{exc} = 520 nm, λ_{em} = 540 nm) and b) UC mode excitation (λ_{exc} = 980 nm, λ_{em} = 540 nm); red emission from Er^{3+} $^4F_{9/2}\rightarrow{}^4I_{15/2}$ using c) direct excitation (λ_{exc} = 649 nm, λ_{em} = 654 nm) and d) UC mode excitation (λ_{exc} = 980 nm, λ_{em} = 654 nm); NIR emission from Er^{3+} $^4I_{13/2}\rightarrow{}^4I_{15/2}$ using e) direct excitation (λ_{exc} = 1500 nm, λ_{em} = 1530 nm) and f) UC mode excitation (λ_{exc} = 980 nm, λ_{em} = 1530 nm).

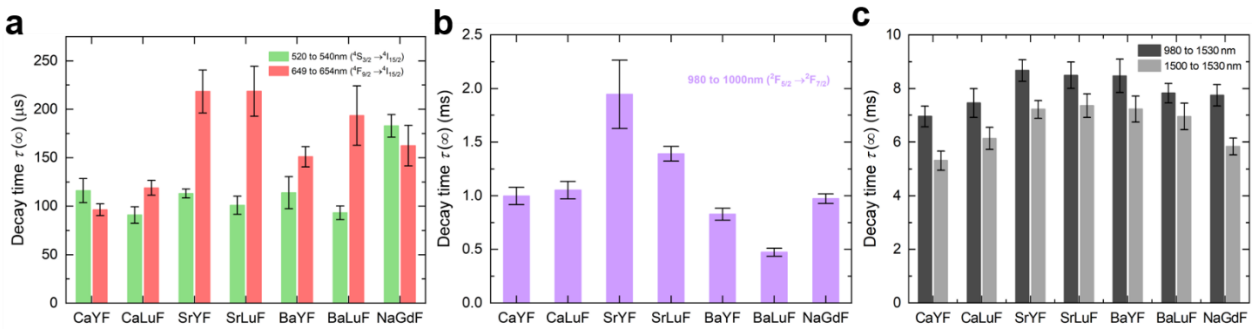

Figure S36. Absolute values of the decay times for infinite shell thickness (d→∞) as determined by fitting Equation 2 from the main text to the decay times as a function of shell thickness. a) Decay time of the green (Er^{3+} $^4S_{3/2}$→$^4I_{15/2}$) and red (Er^{3+} $^4F_{9/2}$→$^4I_{15/2}$) emission using direct excitation of the corresponding energy levels. b) Decay time of the Yb^{3+} $^2F_{7/2}$→$^2F_{5/2}$ transition under direct 980 nm excitation and 1000 nm emission. c) Decay time of the NIR Er^{3+} $^4I_{13/2}$→$^4I_{15/2}$ transition around 1530 nm under direct excitation at 1500 nm and 980 nm excitation.

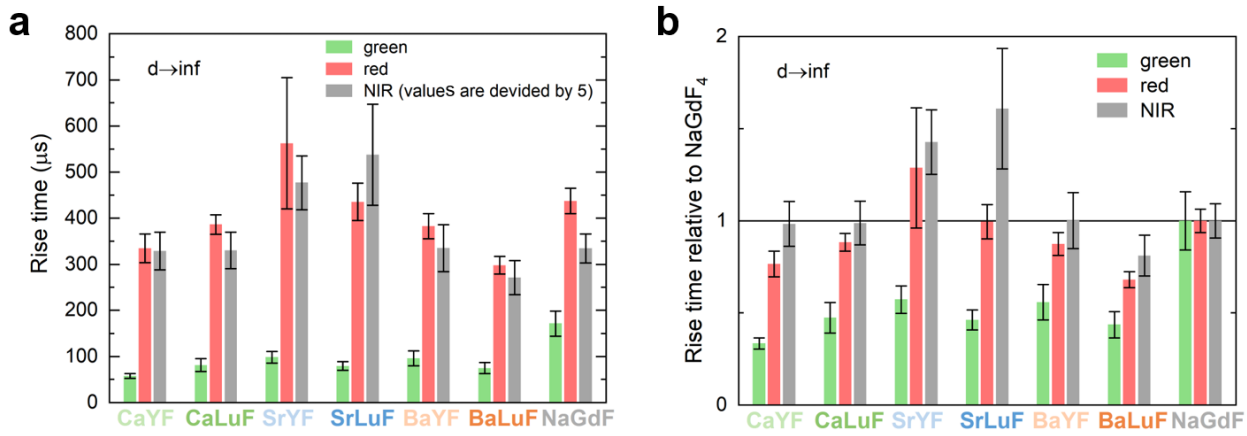

Figure S37. a) Absolute rise time values for infinite shell thickness (d→∞) as determined by fitting Equation 2 from the main text to the rise time values as a function of shell thickness. b) Rise time for infinite shell thickness relative to the values determined for NaGdF. Besides Sr-based samples, all MLnF compounds show shorter rise times compared to NaGdF for the green (Er^{3+} $^4S_{3/2}$→$^4I_{15/2}$) and red (Er^{3+} $^4F_{9/2}$→$^4I_{15/2}$) transition under 980 nm excitation. Sr-based samples have also long rise times for NIR emission of Er^{3+} $^4I_{13/2}$→$^4I_{15/2}$ under 980 nm excitation.

3.3 Literature comparison of upconversion quantum yield measurements

Table S4. List of UCQY values reported in literature for core/shell upconverting nanoparticles with similar core sizes, shell thickness, and irradiance of the 980 nm excitation. The distribution of literature values highlights the challenging UCQY measurements of ultra-small UCNPs.

Material	Size (nm)	UCQY (%)	Comments	Ref
$NaYF_4$:Yb,Er (20:2) @$NaYF_4$	**17** core: 5 shell: 6	**0.5 @100W/cm²**	Taken from a Table	5
$NaYF_4$:Yb,Er (20:2) @$NaYF_4$	**14** core: 8 shell: 3	**0.5 @100W/cm²**	Taken from a Table	6
$NaGdF_4$:Yb,Er (20:2)@$NaYF_4$	**16** core: 4 shell: 6	**~0.3 @100W/cm²**	Extracted from Figure	3
$NaGdF_4$:Yb,Er (20:2)@$NaYF_4$	**11.7** core: 4.8 shell: 3.5	**~0.55 @100W/cm²**	Extracted from Figure	7
$NaGdF_4$:Yb,Er (18:2)@$NaYF_4$	**16** core: 5.5 shell: 5.2	**~0.22 @100W/cm²**	Extrapolated data from Figure 2d to 100 W/cm²	this study
SrLuF:Yb,Er(30.6:2.9)@SrLuF	**~11 edge length** core: 4.9 shell: ~4	**~0.66 @100W/cm²** **(0.53 @80 W/cm²)**	Extrapolation from 80 to 100 W/cm², Figure 3d 13.6 nm with 4.4 nm shell when converted to sphere (see Table S3)	this study
SrLuF:Yb,Er(30.6:2.9)@SrLuF	**~16** core: 4.9 shell: ~5.5	**~1.0 @100W/cm²**	Extrapolation of data from Figure 3c and Figure 3d	this study

References

(1) Fischer, S.; Swabeck, J. K.; Alivisatos, A. P. Controlled Isotropic and Anisotropic Shell Growth in β-$NaLnF_4$ Nanocrystals Induced by Precursor Injection Rate. *J. Am. Chem. Soc.* **2017**, *139* (35), 12325–12332.

(2) Chen, C.; Liu, J.; Chen, Y.; Li, C.; Liu, X.; Huang, H.; Liang, C.; Lou, Y.; Shi, Z.; Feng, S. Sub-10 Nm Sr_2LuF_7:Yb/Er@Sr_2GdF_7@SrF_2 Up-Conversion Nanocrystals for Up-Conversion Luminescence–Magnetic Resonance–Computed Tomography Trimodal Bioimaging. *ACS Appl. Mater. Interfaces* **2017**, *9* (7), 5748–5756.

(3) Würth, C.; Fischer, S.; Grauel, B.; Alivisatos, A. P.; Resch-Genger, U. Quantum Yields, Surface Quenching, and Passivation Efficiency for Ultrasmall Core/Shell Upconverting Nanoparticles. *J. Am. Chem. Soc.* **2018**, *140* (14), 4922–4928.

(4) Fischer, S.; Bronstein, N. D.; Swabeck, J. K.; Chan, E. M.; Alivisatos, A. P. Precise Tuning of Surface Quenching for Luminescence Enhancement in Core–Shell Lanthanide-Doped Nanocrystals. *Nano Lett.* **2016**, *16* (11), 7241–7247.

(5) Li, X.; Shen, D.; Yang, J.; Yao, C.; Che, R.; Zhang, F.; Zhao, D. Successive Layer-by-Layer Strategy for Multi-Shell Epitaxial Growth: Shell Thickness and Doping Position Dependence in Upconverting Optical Properties. *Chem. Mater.* **2013**, *25*, 106–112.

(6) Gargas, D. J.; Chan, E. M.; Ostrowski, A. D.; Aloni, S.; Altoe, M. V. P.; Barnard, E. S.; Sanii, B.; Urban, J. J.; Milliron, D. J.; Cohen, B. E.; et al. Engineering Bright Sub-10-Nm Upconverting Nanocrystals for Single-Molecule Imaging. *Nat. Nanotechnol.* **2014**, *9* (4), 300–305.

(7) Hudry, D.; Busko, D.; Popescu, R.; Gerthsen, D.; Abeykoon, A. M. M.; Kübel, C.; Bergfeldt, T.; Richards, B. S. Direct Evidence of Significant Cation Intermixing in Upconverting Core@Shell Nanocrystals: Toward a New Crystallochemical Model. *Chem. Mater.* **2017**, *29* (21), 9238–9246.